

## A Very Deep *Chandra* View of Abell 2597: Multiple Signatures of AGN Activity, Shocks, Cold Fueling, and a Plasma Depletion Layer

OSASE OMORUYI ,<sup>1</sup> GRANT TREMBLAY ,<sup>1</sup> STEFI A. BAUM ,<sup>2</sup> TRACY CLARKE ,<sup>3</sup> PRATIK DABHADE ,<sup>4</sup>  
MASSIMO GASPARI ,<sup>5</sup> SANNA GULATI ,<sup>6</sup> PREETI KHARB ,<sup>6</sup> MAXIM MARKEVITCH ,<sup>7</sup> PAUL NULSEN ,<sup>1</sup>  
CHRISTOPHER P. O'DEA ,<sup>2</sup> SCOTT RANDALL ,<sup>1</sup> SOMAK RAYCHAUDHURY ,<sup>8</sup> SRAVANI VADDI ,<sup>9</sup> ALEXEY VIKHLININ ,<sup>1</sup>  
JOHN ZUHONE ,<sup>1</sup> AND FRIENDS :)

<sup>1</sup>Center for Astrophysics | Harvard & Smithsonian, 60 Garden St., Cambridge, MA 02138, USA

<sup>2</sup>University of Manitoba, Dept. of Physics and Astronomy, Winnipeg, MB R3T 2N2, Canada

<sup>3</sup>U.S. Naval Research Laboratory, 4555 Overlook Avenue SW, Washington, DC 20375, USA

<sup>4</sup>Astrophysics Division, National Centre for Nuclear Research, Pasteura 7, 02-093 Warsaw, Poland

<sup>5</sup>Department of Physics, Informatics & Mathematics, University of Modena & Reggio Emilia, 41125 Modena, Italy

<sup>6</sup>National Centre for Radio Astrophysics, Tata Institute for Fundamental Research, Savitribai Phule Pune University, Ganeshkhind, Pune 411007, India

<sup>7</sup>NASA Goddard Space Flight Center, Code 662, Greenbelt, MD 20771

<sup>8</sup>Ashoka University, Dept. Of Physics, Sonipat, Haryana-131029, India

<sup>9</sup>Arecibo Observatory, NAIC, HC3 Box 53995, Arecibo, Puerto Rico, PR 00612, USA

### ABSTRACT

We present deep ( $\sim 600$  ks) *Chandra* X-ray observations, complemented by archival GMRT radio and SINFONI near-infrared data, to investigate how AGN-driven outflows shape the intracluster medium and sustain black hole accretion in the cool-core galaxy cluster Abell 2597. Radio AGN activity has inflated six X-ray cavities and driven three potential shock fronts ( $\mathcal{M} \sim 1.07\text{--}1.14$ ) extending out to 150 kpc, suggesting recurrent outbursts with a duty cycle of  $\sim 10^7$  years. This feedback has left distinct imprints on the ICM: the smallest, innermost cavity is surrounded by cool, low-entropy gas, while the largest cavity is enshrouded by warmer, high-entropy gas. Metal-enriched gas is preferentially aligned with the radio jet axis, and an elongated X-ray surface brightness deficit is detected, likely shaped by sloshing motions that amplified magnetic fields and/or displaced gas within the cluster core. Despite AGN feedback injecting  $\sim 10^{44}$  erg s $^{-1}$ , comparable to the cluster's cooling luminosity, radiative cooling persists at  $\sim 15$  M $_{\odot}$ yr $^{-1}$ , replenishing a  $\sim 3.2 \times 10^9$  M $_{\odot}$  cold molecular gas reservoir. Sustaining this level of AGN activity requires a continuous fuel supply, yet the estimated Bondi accretion power ( $\sim 2 \times 10^{43}$  erg s $^{-1}$ ) falls an order of magnitude short of the observed cavity power. Instead, ALMA observations continue to support a chaotic cold accretion scenario, where turbulence-driven condensation fuels the AGN at rates exceeding Bondi accretion. These infalling cold clouds serve as the primary feeding mechanism for AGN activity, sustaining the self-regulated feedback cycle that repeatedly shapes the core of Abell 2597.

*Keywords:* galaxies: clusters: individual: Abell 2597 - X-rays: galaxies: clusters.

### 1. INTRODUCTION

Galaxy clusters, the largest gravitationally bound structures in the Universe, consist of hundreds to thousands of galaxies embedded in a vast expanse of hot ( $\sim 10^7$  –  $10^8$  K) and diffuse plasma known as the intracluster medium (ICM). Approximately half of all clusters exhibit a distinct feature known as a “cool core,” where the central region hosts an overdensity of rapidly cooling, X-ray-bright gas. As the gas cools, it loses

pressure support, resulting in a continuous inflow of cooler, multiphase gas toward the central brightest cluster galaxy (BCG). In the classic “cooling flow” model, this process should fuel star formation rates of up to several hundred solar masses per year near the cluster core. However, observations consistently fail to detect such extreme star formation, suggesting that the remaining cooling is hidden from view (e.g., Fabian et al. 2022, 2023), and/or some mechanism, most likely mechanical feedback from the supermassive black hole at the cen-

ter of the BCG, must be counteracting the cooling flow (Veilleux et al. 2005; McNamara & Nulsen 2007; Fabian 2012; McNamara & Nulsen 2012; Kormendy & Ho 2013; Gaspari et al. 2020, for reviews).

Abell 2597 ( $z = 0.0821$ ), a nearby cool-core galaxy cluster, serves as a canonical example of AGN feedback regulating cooling in cluster cores, preventing extreme star formation in BCGs and contributing to the steep decline in the galaxy luminosity function at high luminosities (Bower et al. 2006; Croton et al. 2006). Within the cluster’s rapidly cooling hot atmosphere, the BCG’s SMBH expels powerful radio jets, inflating a  $\sim 30$  kpc network of buoyantly rising bubbles observed as X-ray ‘cavities’ (Tremblay et al. 2012a). As the bubbles rise and expand, they heat the surrounding plasma (Churazov et al. 2002; Tremblay et al. 2012a), reducing the classical cooling flow rate from  $\sim 500 \text{ M}_\odot \text{yr}^{-1}$  to  $\sim 20\text{--}75 \text{ M}_\odot \text{yr}^{-1}$ , as measured by O VI ultraviolet emission tracing  $\sim 7 \times 10^5 \text{ K}$  gas (Oegerle et al. 2001). In addition to mitigating intracluster gas cooling, these bubbles likely uplifted the  $\sim 30$  kpc multiphase filamentary nebula observed in the cluster core (Tremblay et al. 2012b, 2018).

Recent Atacama Large Millimeter/submillimeter Array (ALMA) CO(2-1) observations of the BCG’s cold gas revealed three redshifted ( $+300 \text{ km s}^{-1}$ ) absorption lines against the SMBH’s mm-synchrotron continuum, tracing infalling clouds delivering  $\sim 0.1$  to a few  $M_\odot \text{yr}^{-1}$  of gas to the black hole (Tremblay et al. 2016). These observations are consistent with recent theoretical advances showing that the fueling of SMBHs in cool-core clusters may be predominantly driven by turbulent cold clouds via chaotic cold accretion (Gaspari et al. 2013, 2017) rather than hot accretion flows (Bondi 1952). Regardless of the dominant accretion phase, the inflowing gas fuels the next round of AGN activity, driving jets and bubbles that uplift cool, low-entropy gas, sustaining a long-lived, self-regulating, galaxy-spanning “fountain” with the black hole acting as its “pump” (Tremblay et al. 2018).

To map the hot phase of the billion solar mass fountain, Tremblay et al. (2012a) analyzed  $\sim 120$  ks of *Chandra* data, revealing a highly anisotropic surface brightness distribution of the ICM and an extended 30 kpc network of X-ray cavities. The largest cavity,  $\sim 25$  kpc in projected length, aligns with 330 MHz radio emission. X-ray spectral maps also revealed a distinct arc of hot, high-entropy gas bordering the inner edge of this cavity. Given the morphology of the feature, they found it unlikely to be a shock or cold front, and instead potentially caused by  $\sim$  keV gas rushing inward to refill the wake left by the buoyantly rising cavity, thermalizing cavity enthalpy and heating the surrounding ICM. However, the

limited depth of the X-ray data prevented a definitive conclusion.

Deep *Chandra* observations, often spanning hundreds of kiloseconds (ks) to megaseconds, have been instrumental in examining the imprints AGN feedback leaves on the hot ICM. These long exposures have led to the discovery of multiple generations of cavities (e.g., Perseus, A2052 Fabian et al. 2003; Blanton et al. 2011), weak shock fronts surrounding powerful outbursts (e.g., Hydra A, NGC 5813, Cygnus A, MS 0735.6+7421, Abell 2052, Hercules A Nulsen et al. (2005); Randall et al. (2015); Snios et al. (2018); Liu et al. (2019); Ubertosi et al. (2024)), and in extreme cases, ripples—interpreted as multiple weak shock fronts—propagating outward into the large-scale ICM (e.g., Perseus Fabian et al. 2006), while also examining the role of hot gas in fueling AGN activity (Russell et al. 2013a, 2015; Bambic et al. 2023).

Building on this legacy of deep *Chandra* observations, this work presents an additional 480 ks of data for Abell 2597, increasing the total exposure time to 590 ks. To complement this dataset, we also tangentially present archival low-frequency radio observations from the Giant Metre Radio Telescope (GMRT), and near-infrared integral field unit observations from the Spectrograph for INtegral Field Observations in the Near Infrared (SINFONI). This paper is structured as follows: Section 2 describes the deep X-ray data and archival radio, ultraviolet, and near-infrared observations used; Section 3 presents a comprehensive description of both newly identified and previously reported structures in the ICM; Sections 4 and 5 examine the heating and cooling balance within the cluster, fuel sources for the SMBH, and the potential origin of the features observed. In this work, we adopt  $H_0 = 70 \text{ km s}^{-1} \text{ Mpc}^{-1}$ ,  $\Omega_M = 0.27$ , and  $\Omega_\Lambda = 0.73$ . At the redshift of the BCG,  $1''$  corresponds to 1.549 kpc, with angular size and luminosity distances of 319.4 Mpc and 374.0 Mpc, respectively, and a Universe age of 12.78 Gyr. Unless stated otherwise, all images are centered on the A2597 BCG nucleus at R.A. 23h 25m 19.7s, Decl.  $-12^\circ 07' 27''$  (J2000), with east left and north up.

## 2. OBSERVATIONS AND DATA REDUCTION

Below, we describe all new and archival observations of Abell 2597 used in this study and also summarize them in Table 1. To ensure transparency and reproducibility, all Python codes and Jupyter Notebooks used for data analysis are publicly available.<sup>1</sup>

<sup>1</sup> [https://github.com/osaseo/abell\\_2597\\_chandra](https://github.com/osaseo/abell_2597_chandra)

**Table 1.** SUMMARY OF ABELL 2597 OBSERVATIONS

Waveband/Line (1)	Facility (2)	Instrument/Config. (3)	Exp. Time (4)	Prog./Obs.ID (Date) (5)	Reference (6)
X-ray (0.2 - 10 keV)	<i>Chandra</i>	ACIS-S/VFAINT	52.20 ks	6934 (2006 May 1)	Tremblay et al. (2012a, 2012b)
...	...	...	60.11 ks	7329 (2006 May 4)	Tremblay et al. (2012a, 2012b)
...	...	...	69.39 ks	19596 (2017 Oct 8)	(Large Program 18800649)
...	...	...	44.52 ks	19597 (2017 Oct 16)	...
...	...	...	14.34 ks	19598 (2017 Aug 15)	...
...	...	...	24.73 ks	20626 (2017 Aug 15)	...
...	...	...	20.85 ks	20627 (2017 Aug 17)	...
...	...	...	10.92 ks	20628 (2017 Aug 19)	...
...	...	...	56.36 ks	20629 (2017 Oct 3)	...
...	...	...	53.4 ks	20805 (2017 Oct 5)	...
...	...	...	37.62 ks	20806 (2017 Oct 7)	...
...	...	...	79.85 ks	20811 (2017 Oct 21)	...
...	...	...	62.29 ks	20817 (2017 Oct 19)	...
<i>K</i> -band	VLT	SINFONI + AO	3600 s	093.B-0638(C) (2014 Jul 19)	this paper
FUV	HST	COS G140L	13952.640 s	30-Oct 2014	Vaddi et al (in prep)
Radio	GMRT	Band 3	85 mins	05DAG01 (20-Mar 2004)	this paper
...	...	Band 4	1969 mins	19_010 (20-Dec 2010)	this paper

NOTE—Summary of all new and archival observations of Abell 2597 presented in this paper. The observations are presented in descending order of wavelength, from X-ray through radio. (1) Waveband or Line Name targeted by the observation; (2) telescope used; (3) instrument (and aperture/detector) used for observation; (4) on-source exposure time; (5) date of observation; (6) reference to publication(s) where the listed data first appeared or were otherwise discussed in detail.

### 2.1. *Chandra* X-ray Observations

As part of Cycle 18 program 18800649 (PI: Tremblay), the *Chandra* X-ray Observatory observed Abell 2597 for a total of 474.3 ks in August and October 2014 (ObsIDs 19596, 19597, 19598, 20626, 20627, 20628, 20629, 20805, 20806, 20811, and 20817). We also included 112.3 ks from two older, previously published observations (ObsIDs 6934 and 7329, PI: Clarke; McNamara et al. 2001; Clarke et al. 2005; Tremblay et al. 2012a,b), leading to a total of 586.6 ks across all fourteen ACIS-S observations. The ObsIDs were processed using the latest versions of CIAO v4.16 (*Chandra* Interactive Analysis of Observations; Fruscione et al. 2006) and CALDB v4.11.5. Data were reprocessed with *chandra\_repro*, and flares were identified and filtered using the CHIPS routine LC\_CLEAN. Few significant flares were detected, leading us to reject a minimal 2.76 ks. Point sources were identified using a wavelet decomposition technique (Vikhlinin et al. 1998), inspected, and masked.

Although A2597 remains a steady source of X-rays, the ACIS optical blocking filter has degraded over time, leading to significant contaminant buildup. Consequently, the earlier *Chandra* observations used have count rates nearly twice as high as those obtained a decade later. This explains why, despite having nearly half the exposure time of the nearby Perseus cluster—where 890 ks of data yielded almost 70 million counts (Fabian et al. 2006)—the  $\sim 600$  ks of obser-

vations for Abell 2597 have produced only 2.1 million counts within  $r_{500} = 592''$ .

#### 2.1.1. Imaging

To create X-ray images of the ICM, we merged the ObsIDs with the MERGE\_OBS CIAO script. Figure 1 presents the resulting merged observations out to  $r_{500}$  (green dashed circle) at *Chandra*'s native  $0''.5$  resolution, corresponding to a physical scale of  $\sim 0.75$  kpc.

To enhance the visibility of subtle features, we constructed an adaptively smoothed surface brightness map using a variable-width Gaussian kernel, requiring that each smoothed region contained at least 100 counts. The resulting X-ray image is overlaid on a false-color ( $z, r, i$ ) PanSTARRS optical image of the cluster's central  $550 \times 340$  kpc region in the lower panel of Figure 1. All X-ray surface brightness contours in this work are derived from this adaptively smoothed image.

To further improve the visibility of structures within the central 180 kpc of the cluster (dashed cyan circle), we applied a gaussian gradient magnitude (GGM) filter and an adaptive GGM filter to the merged image (with point sources removed) using the publicly available code<sup>2</sup> referenced in Sanders et al. (2016) and Sanders et al. (2022). We also created an unsharp-masked image by smoothing the data with a  $0''.98$  Gaus-

<sup>2</sup> <https://github.com/jeremysanders/ggm>

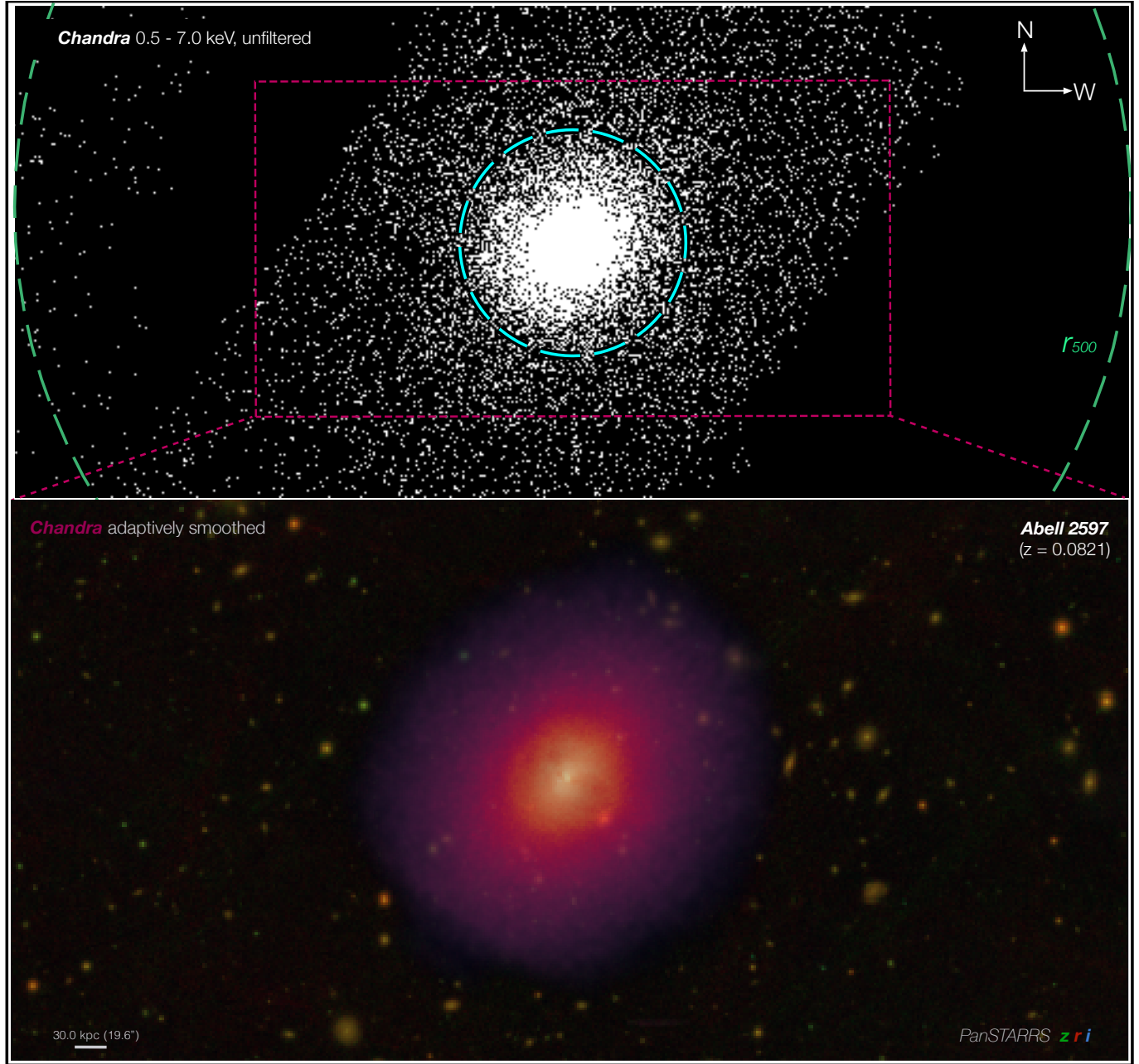


**Figure 1.** *Top:* Background-subtracted, exposure-corrected 0.5-7 keV image of all merged *Chandra* observations for Abell 2597 (see Table 1) out to  $r_{500}$  (green dashed circle). *Bottom:* PanSTARRS  $z$ ,  $r$ ,  $i$  image of the central  $\sim 550 \times 340$  kpc of the cluster overlaid with an adaptively smoothed version of the merged *Chandra* observations.

sian and subtracting it from a version of the image smoothed with a  $9''8$  Gaussian (e.g., Hlavacek-Larrondo et al. 2012).

### 2.1.2. Spectral Profiles

To derive the large-scale spectral properties of A2597’s ICM (e.g.  $M_{500}$ ,  $R_{500}$ ), we followed the methodology presented in Vikhlinin et al. (2006). A full description of this process is provided in Section 2.3 of Omoruyi et al. (2023), where it was applied to SDSS J1531+3414.

In brief, we extracted spectra from concentric annuli centered on the X-ray peak of the cleaned data from the central  $8''.5$  to  $r_{500}$ . Background estimates were obtained from each ObsID’s corresponding blank-sky event file, using the same region as the source. The profile was modeled with the modified  $\beta$ -model from Vikhlinin et al. (2006) (Equation 3). From the best-fit model, we derived the three-dimensional gas density  $\rho_g(r)$  to compute the total gas mass  $M_g$  and estimate the classical cooling rate  $\dot{M}_{\text{cool}}$ .

A large-scale temperature profile was obtained using 12 logarithmically spaced annuli extending to  $r_{500}$ , with each annulus containing at least 74,000 net counts after background subtraction. The temperature was modeled using the three-dimensional analytic form from Equation 6 in Vikhlinin et al. (2006) and then projected. Using the derived temperature and gas density profiles, we calculated the total cluster mass within radius  $r$  under the assumption of hydrostatic equilibrium (Sarazin 1988), and adopted  $M_{500}$  and  $R_{500}$  from the  $Y_X$ - $M$  scaling relation (Vikhlinin et al. 2009).

To better examine features in the cluster core, we extracted spectra from 30 linearly spaced concentric annuli extending to  $\sim 180$  kpc, marked by the cyan circle in Figure 1. For each ObsID, spectra were extracted in the 0.5–7 keV range, with background subtraction performed using blank-sky files.

The spectra were fit with a PHABS\*APEC model in XSPEC, fixing  $N_H = 2.252 \times 10^{20} \text{ cm}^{-2}$  (Bekhti et al. 2016) and  $Z = 0.3Z_\odot$  (e.g., Panagoulia et al. 2014), while allowing  $kT$  and the normalization  $N(r)$  to vary. The fitted values were used to derive the deprojected electron density profile, assuming spherical symmetry, from which the pressure  $P \equiv 1.83n_e kT$  and entropy  $K \equiv kTn_e^{-2/3}$  were computed. To fit the radial abundance profile, we followed the same approach but reduced the number of annuli from 30 to 15 for improved sensitivity, and allowed the abundance to vary as a free parameter.

### 2.1.3. Spectral Maps

To generate high-resolution temperature, pressure, and entropy maps, we applied the Contour Binning algorithm (Sanders 2006), which groups pixels along surface brightness contours until a specified signal-to-noise threshold is met. Using an adaptively smoothed, point-source-free image ( $S/N = 15$  in the 0.5–7 keV band), the algorithm identified 1789 spatial bins with a minimum S/N of 30, corresponding to  $\sim 900$  net counts per bin. A geometric constraint factor of  $C = 2$  was used to ensure compact bin shapes. We then used J. Sanders’ `make_region_files` to create CIAO-compatible region files, extracting spectra for each bin across all ObsIDs and estimating the background from the corresponding blank-sky files. The summed spectra were fit simultaneously in XSPEC using an absorbed MEKAL model, with redshift, Galactic  $N_H$ , and metallicity fixed to the same values used in the spectral profile fitting.

Using the best-fit temperature  $kT$  and normalization  $N(r)$ , we constructed projected temperature, entropy, and pressure maps with J. Sanders’ `paint_output_images`. The temperature map was derived directly from  $kT$ , while pseudo-entropy and

pseudo-pressure maps assumed the electron density scales as  $\sqrt{N(r)}$ , yielding units of  $\text{keV cm}^{-5/2} \text{ arcsec}^{-1}$  for pressure and  $\text{keV cm}^{5/3} \text{ arcsec}^{2/3}$  for entropy. For the abundance map, we followed the same procedure but increased the minimum S/N per bin to 100 to ensure robust fits. All spectral maps shown only include bins where the fits exceed  $> 5\sigma$ . The resulting deep X-ray image, spectral profiles, and spectral maps are presented in Section 3.

## 2.2. Archival GMRT Radio Observations

Abell 2597 was observed multiple times with the GMRT between 2000 and 2020 at various frequencies: 157 MHz (PI: Somak Raychaudhury), 244 MHz (PI: Tracy Clarke), 311 MHz (PI: Nithyanandan Thyagarajan), 610 MHz (PIs: Vasant Krishna Kulkarni, David Alan Green), 614 MHz (PI: Tracy Clarke), and 629 MHz (PI: Somak Raychaudhury). However, most datasets were severely affected by radio frequency interference, making them unsuitable for spatially resolved analysis. The only recoverable observations were at 244 MHz and 610 MHz. *hello radio friends. are we going to describe what software you used here?*

## 2.3. Archival SINFONI Observations

In 2014, the Spectrograph for INtegral Field Observations in the Near Infrared (SINFONI; Eisenhauer et al. (2003)) on the Very Large Telescope observed the nucleus of A2597. Under ESO Program ID 093.B-0638(C) (PI: Raymond), the near-infrared observations were performed in the K-band filter (1.95–2.45  $\mu\text{m}$ ), providing integral field data cubes covering the  $H_2$  (ro)vibrational lines. The observations were performed using the Laser Guide Star Adaptive Optics (AO) mode (Bonnet et al. 2003). Strap-length limits required that tip/tilt correction, which compensates for small-scale variations in the wavefront caused by atmospheric turbulence and improves spatial resolution, be attempted on the A2597 nucleus. The correction, however, was unsuccessful, for the nucleus lacked sufficient contrast against the blurred galaxy caused by atmospheric conditions. Consequently, the observations were conducted in a “seeing enhancer mode” which enables us to achieve a spatial resolution of 0''.6 (FWHM), only a moderate increase in spatial resolution relative to the previous 1'' seeing-limited images of the nucleus published in Oonk et al. (2010).

The SINFONI-AO data were reduced using ESOREX (3.13.6) workflow 3.3.2 in the EsoReflex environment (Freudling et al. 2013). Emission lines in the resulting data cube were modeled using the spectroscopic analysis toolkit PYSPCKIT (Ginsburg et al. 2022). Continuum emission from the host stellar component was subtracted

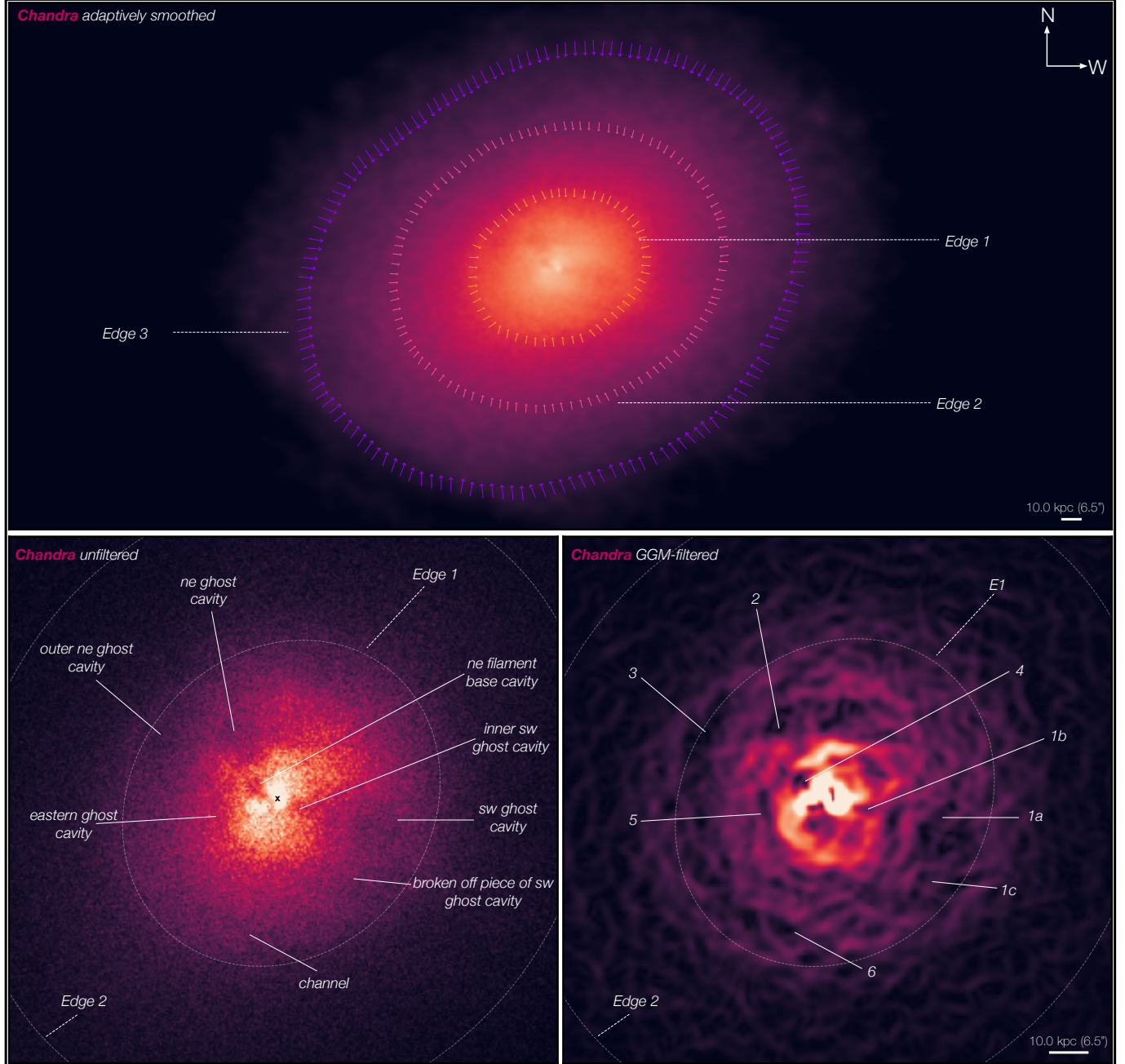


**Figure 2.** Identified features in the ICM of Abell 2597. *Top:* Adaptively smoothed image of the  $\sim 550 \times 340$  kpc cluster environment, highlighting three surface brightness edges (colorful arrows). *Bottom:* Central  $\sim 180 \times 110$  kpc region showing an unfiltered *Chandra* image (left) and a GGM-filtered image (right). Seven cavities and an X-ray channel are identified and labeled. The adaptively smoothed and unfiltered images shown are the same as those shown in Figure 1.

using nearby line-free regions, and the H<sub>2</sub> emission lines were fit with single-component Gaussian profiles.

### 3. THE DEEPEST VIEW OF THE HOT ICM

#### 3.1. *X-ray Morphology and Features*

Figure 2 presents background-subtracted, exposure-corrected *Chandra* X-ray images of Abell 2597 in the 0.5–7.0 keV band. The top panel shows an adaptively

smoothed X-ray image of the cluster's  $\sim 450$  kpc  $\times$  230 kpc environment. The X-ray emission is centrally peaked, characteristic of cool-core clusters, and gradually fades into a diffuse halo. The morphology is broadly anisotropic, with prominent extensions to the northeast and southwest. Additionally, three subtle, nearly elliptical surface brightness edges are observed in the outer cluster regions (marked by dashed white arcs).

**Table 2.** Notable Features in Abell 2597's ICM

Label	Feature	Ref.
E1	Edge 1	New
E2	Edge 2	New
E3	Edge 3	New
1a	SW Ghost Cavity	M01
1b	Inner SW Ghost Cavity	C05
1c	Broken off Piece of SW Ghost Cavity	New
2	NE Ghost Cavity	M01
3	Outer NE Ghost Cavity	T12a, T12b
4	NE Filament Base Cavity	C05
5	Eastern Ghost Cavity	New
6	Channel	New

The most prominent structures lie within the innermost surface brightness edge. To highlight these features, the lower two panels of Figure 1 zoom in on the central  $\sim 75$  kpc ( $50''.0$ ). The X-ray emission around the nuclear region, marked by a cross at its peak, forms a backward ‘S’ shape due to surface brightness deficits to the northeast and southwest. These deficits are labeled alphanumerically, with a full list provided in Table 2.

The first 32 ks *Chandra* X-ray observations of Abell 2597 by McNamara et al. (2001) (hereafter M01) identified two prominent cavities in the ICM: one to the northeast (Feature 2) and one to the southwest (Feature 1a). Their far distances from the central AGN led to their classification as “ghost” cavities, indicative of an older epoch of AGN feedback. Clarke et al. (2005) (hereafter C05) later reanalyzed the same *Chandra* data using residual imaging, revealing a possible ‘tunnel’ (Feature 1b) connecting the southwestern cavity to the central radio source. However, its nature remained uncertain, as it could either be a distinct structure or part of a larger cavity encompassing the M01 cavity.

Deeper *Chandra* observations, with nearly four times the prior exposure time (120 ks), presented in Tremblay et al. (2012a,b) (hereafter T12a and T12b) discovered that the network of X-ray cavities was more extended than previously thought. Notably, the western ghost cavity described by M01 and C05 appeared to be part of a larger, teardrop-shaped cavity extending  $\sim 25$  kpc in projected length, referred to here as the southwestern ghost cavity (Features 1a and 1b). T12b also identified an additional northeastern ghost cavity (Feature 3).

With our additional 480 ks of data, we find that the previously identified structures extend even further than previously reported. The southwestern cavity now appears connected to a surface brightness deficit directly below it (Feature 1c), which may be a sheared-off por-

tion of the original cavity. Additionally, we identify a potential new ghost cavity to the east of the X-ray peak (Feature 5), roughly opposite the southwestern cavity. Whether the eastern cavity extends northeastward toward the previously identified northeastern ghost cavity (Feature 3) remains uncertain, leaving open the possibility that it shares an elongated morphology similar to the southwestern cavity. Lastly, we also identify a thin, elongated surface brightness depression to the south (Feature 6). Given its morphology, we tentatively classify it as an X-ray brightness “channel,” similar to structures observed in Abell 520 and Abell 2142 (Wang et al. 2016; Wang & Markevitch 2018).

The extensive AGN feedback activity in the cluster core may be linked to the large-scale edges seen in the top panel of Figure 2. If real, these edges could mark an expanding “cocoon” shock, formed by the backflow of the ICM around AGN-inflated bubbles. Due to their faintness, such cocoons are typically observed in clusters with deep exposures (e.g. Hydra A (Nulsen et al. 2005), Cygnus A (Snios et al. 2018), and RBS 797 (Ubertosi et al. 2023)), though similar features have also been detected in shallower *Chandra* observations (e.g. MS 0735.6+7421 (Vantyghem et al. 2014) and 3C 88 (Liu et al. 2019)). We further investigate the nature of this potential AGN-driven cocoon shock in Section 3.4.1.

### 3.2. Jet-ICM Interaction

Abell 2597 is not only home to an extensive network of X-ray cavities but also a complex system of radio sources spanning multiple frequencies. Figure 3 presents a multi-frequency comparison of the radio continuum and X-ray emission in Abell 2597.

The top panel overlays VLA radio contours at 330 MHz, 1.3 GHz, and 8.4 GHz onto X-ray images binned at 4, 2, and 0.5 pixels, showing how both high-frequency emission from recent jet activity and low-frequency emission from aged plasma correlate with the X-ray structures. C05 found that the 330 MHz radio emission, which traces older, more extended plasma, is cospatial with the entire southwestern cavity. We note that the edges of the 330 MHz source also lie just inside the large-scale surface brightness edge, suggesting it may be driving the expansion of the potential shocked cocoon.

While the older radio plasma aligns with the outer cavities, the younger plasma primarily traces the inner cavities. The 1.3 GHz and 8.4 GHz radio sources are directly connected to the northeastern filament base cavity and the inner southwestern ghost cavity. Additionally, the large-scale 1.3 GHz emission coincides with a bright X-ray filament between the northern and eastern cavities. As noted by T12a, this alignment suggests that

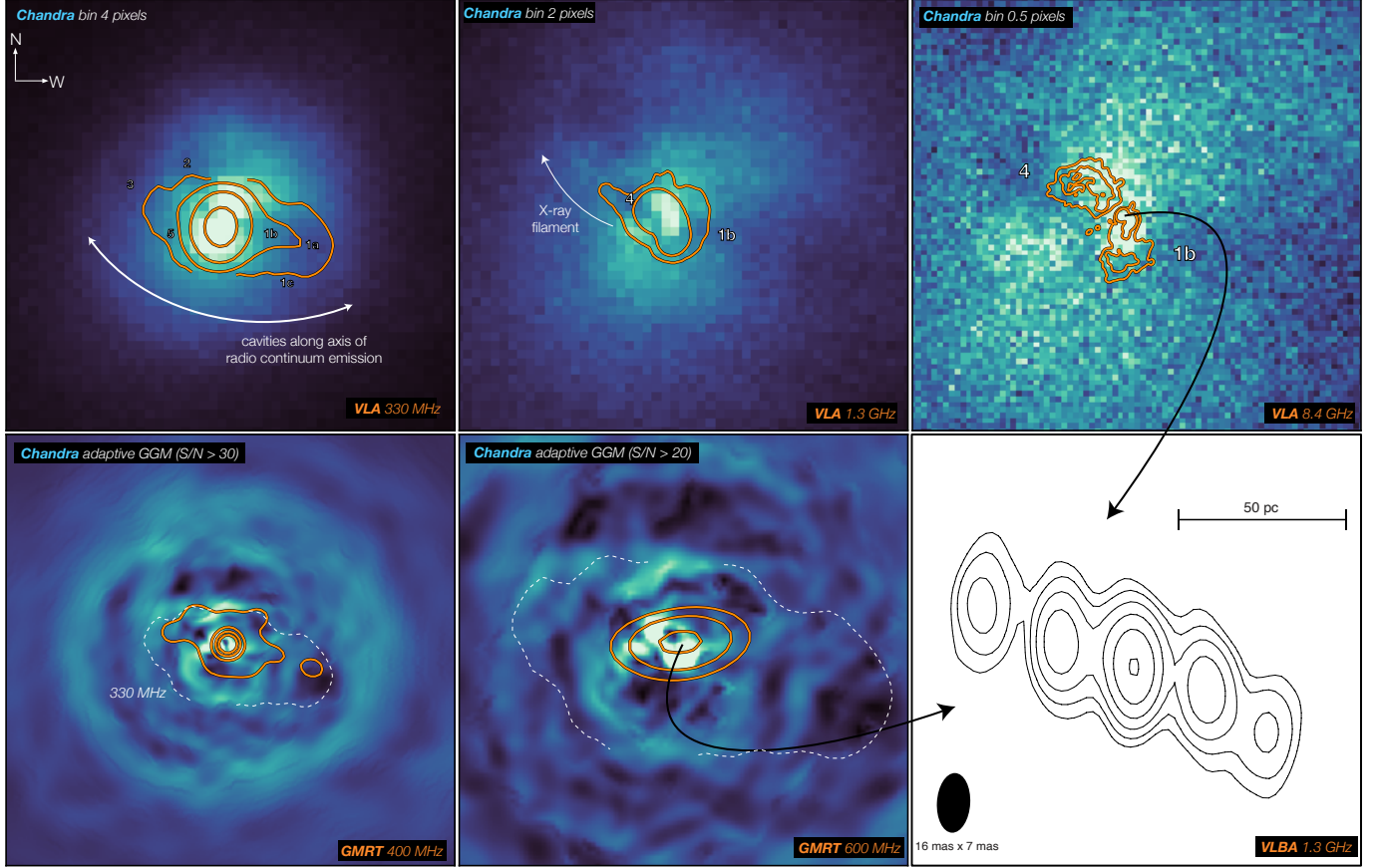


**Figure 3.** X-ray (blue) and radio (orange contours) comparison within the cluster’s central 75 kpc. *Top:* X-ray images binned at 4, 2, and 0.5 pixels, overlaid with VLA radio contours at 330 MHz, 1.3 GHz, and 8.4 GHz. *Bottom:* Adaptive GGM-filtered X-ray images with  $S/N \sim 20$  (left) and  $S/N \sim 30$  (center), overlaid with GMRT 400 MHz (left) and 600 MHz (center) contours. The right panel shows a zoomed-in  $\sim 70$  pc view of the cluster, featuring the ultra-high-resolution archival 1.3 GHz VLBA continuum map, which reveals the jet’s orientation at launch. All cavities align with the axes of the radio continuum emission.

past jet activity may have uplifted cooler, denser gas along this direction.

The lower left panels of Figure 3 overlay archival GMRT 400 MHz and 600 MHz radio contours on adaptively smoothed, GGM-filtered X-ray images. The 400 MHz emission closely follows the 330 MHz source but is slightly more compact. A key exception is its northeastern extension, where it overlaps more with the northeastern ghost cavity than the 330 MHz emission, suggesting a common origin. The 600 MHz emission is similarly contained within the 330 MHz source but does not fully encompass it, instead extending toward the northern cavity and the base of the southwestern teardrop cavity.

The lower right panel of Figure 3 provides a high-resolution VLBA 1.3 GHz view of the central 70 pc, offering a direct look at the jet’s orientation at launch. While the 8.4 GHz emission traces younger plasma, the VLBA data probe smaller scales, capturing the jet’s initial trajectory. Across all frequencies, the jet direction remains largely consistent, oriented northeast to south-

west, with all identified cavities closely aligning with the axes of the radio continuum emission.

### 3.3. Thermodynamic Profiles of the ICM

We present thermodynamic profiles of the ICM in Figures 4 and 5. Key X-ray properties, including the total cluster mass  $M_\Delta$ , radius  $R_\Delta$ , central temperature  $kT_0$ , central entropy  $K_0$ , and central pressure  $P_0$  are listed in Table 3.

The projected emission measure profile (Figure 4) confirms the central excess characteristic of cool-core clusters. The modified  $\beta$ -model from Vikhlinin et al. (2006) (red line) provides a good overall fit, though deviations appear within the central 60 kpc (grey-shaded region), as shown in the inset panel, where surface brightness fluctuations coincide with X-ray cavities. At low redshift, cool-core clusters typically exhibit central cusps in their X-ray surface brightness distributions. Vikhlinin et al. (2007) characterized these cusps using the power-law index of the gas density profile,  $\alpha = -2, d \log \rho_g / d \log r$ , evaluated at  $r = 0.04R_{500}$ . Clusters

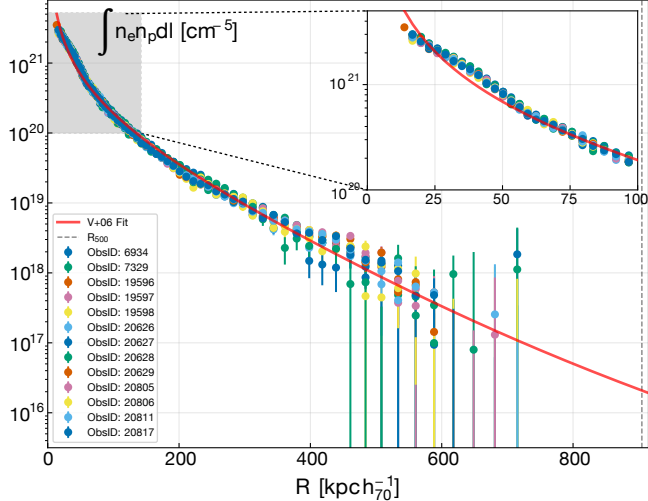


**Figure 4.** X-ray emissivity per unit area for all *Chandra* ObsIDs (colorful points), fit with a modified beta model (red line) from [Vikhlinin et al. \(2006\)](#).

**Table 3.** THERMODYNAMIC PROPERTIES

Property (units)	Value
$M_{500} - Y_X (10^{14} M_\odot)$	$2.28 \pm 0.018$
$R_{500}$ (kpc)	$904.8 \pm 2.4$
$R_0$ (kpc)	3.7
$kT_0$ (keV)	$2.23 \pm 0.029$
$Z_0 (Z_\odot)$	$0.30 \pm 0.019$
$K_0$ (keV cm $^2$ )	$7.8 \pm 0.11$
$P_0 (10^{-9} \text{ dyn cm}^{-2})$	$1.08 \pm 0.016$

NOTE—Summary of key X-ray properties of Abell 2597 at a radius of 12.5 kpc.  $M_{500}$  and  $R_{500}$  are calculated assuming hydrostatic equilibrium and the  $Y_X - M$  relation from [Vikhlinin et al. \(2009\)](#) using profiles extracted from log-spaced annuli. The central temperature  $kT_0$ , abundance  $Z_0$ , pressure  $P_0$ , and entropy  $K_0$  are extracted from the finely spaced linear annuli.

with strong cool cores generally have  $\alpha > 0.7$ . While [Vikhlinin et al. \(2007\)](#) previously reported  $\alpha = 1.1$  for A2597, our deeper data reveal a steeper value of  $\alpha = 2.4$ , further confirming the presence of a strong cool core.

Figure 5 shows the thermodynamic profiles within the central 200 kpc, encompassing all the prominent features identified in Figure 2. The projected temperature (top panel) declines toward the core, from 3.75 keV at  $r \sim 100$  kpc to 2.25 keV at the center. Subtle temperature increases within  $2-3\sigma$  are observed at the locations of the surface brightness edges, which are highlighted as dashed lines. While they could indicate real temperature jumps, they may simply reflect the typical outward temperature rise in cool-core clusters rather than true discontinuities.

The abundance profile (upper middle panel) starts at  $0.3Z_\odot$  in the cluster center and peaks at  $\sim$

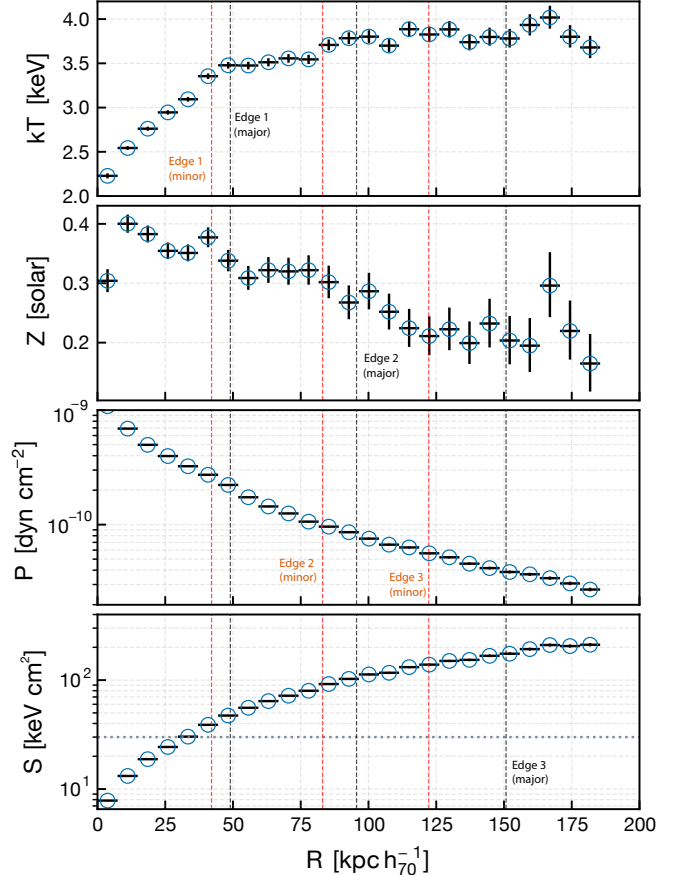


**Figure 5.** Spectral profiles of the ICM within the central 200 kpc. The major (black) and minor (red) axes of each surface brightness edge are marked with dashed lines.

$0.45Z_\odot$  within the X-ray cavity region, consistent with the  $0.5Z_\odot$  metallicity measured for the multiphase gas in the same region via deep optical spectroscopy ([Voit & Donahue 1997](#)). Beyond the cavities, the abundance gradually declines to  $\sim 0.2 Z_\odot$ , but shows a slight ( $\sim 1-2\sigma$ ) increase near the second and third surface brightness edges.

The pressure profile (lower middle panel) follows the expected steep radial decline for a relaxed cluster. The entropy profile (lower panel) falls well below the 30 keV cm $^2$  threshold for star formation in cool-core clusters (dashed line) ([Voit et al. 2008](#)) within the central  $\sim 30$  kpc. At the surface brightness edges, the pressure profile shows  $2-3\sigma$  breaks, while the entropy profile increases smoothly with radius.

### 3.4. Thermodynamic Structure of the ICM

Figure 6 shows the ICM temperature distribution, with the top panel displaying the large-scale structure and the lower panels focusing on the central 75 kpc. On large scales, the gas follows the expected cool-core profile, with the coolest ( $T < 3$  keV) gas concentrated at the center and increasing outward. Similar to the surface

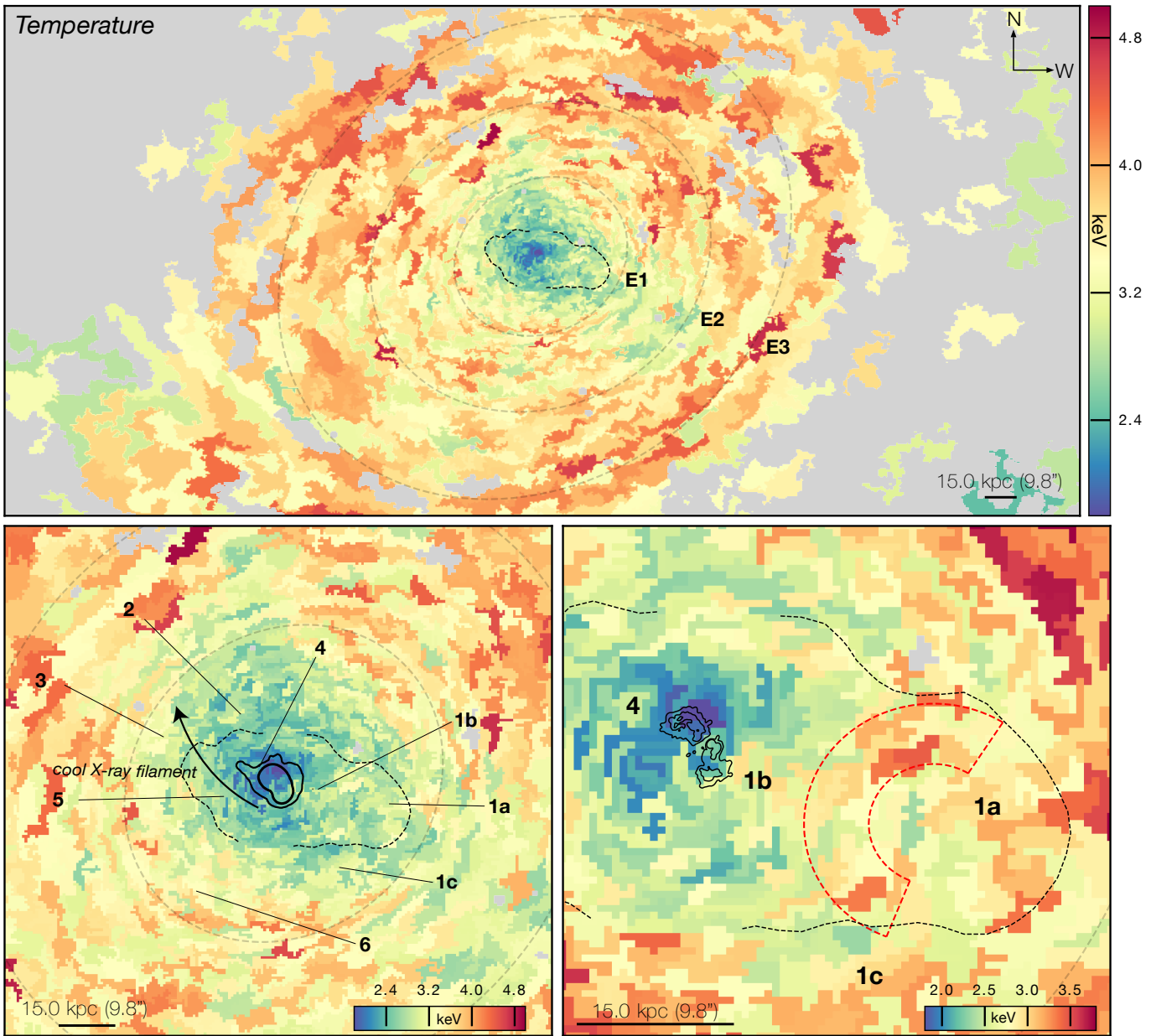


**Figure 6.** Temperature distribution of the ICM. *Top:* Large-scale ( $150 \text{ kpc} \times 200 \text{ kpc}$ ) map revealing a cool ( $T < 3 \text{ keV}$ ) core, with temperature increasing outward. Concentric rings of hotter gas align with surface brightness edges, possibly tracing shocks. *Bottom left:* Zoomed-in view of the central 75 kpc, where cool gas is cospatial with the central X-ray surface brightness distribution, particularly the X-ray filament identified in Figure 3. *Bottom right:* A ring of hot gas, comprising what we label the “hot arc” is visible. *not really arc looks like a full ring*

brightness distribution, the temperature is anisotropic, with cool gas extending along the axes of the 330 MHz radio source (black dashed contours) and to the north. Several concentric rings of elevated temperature coincide with the surface brightness edges identified in Figure 2, potentially marking the boundaries of the expanding shocked “cocoon.”

In the central 75 kpc (lower panels), the coolest ( $T < 2.3 \text{ keV}$ ) gas near the 8.4 GHz radio source follows a backward ‘S’ shape, mirroring the X-ray surface brightness distribution. The northern extension of cool gas aligns with the  $\sim 15 \text{ kpc}$  soft X-ray fila-

ment identified by T12b, which our deeper data show extends even further northeast, reaching  $\sim 18 \text{ kpc}$ . The northeastern filament base cavity (Feature 4), associated with the 8.4 GHz source (black solid contours), contains slightly warmer gas surrounded by a cooler shell. In contrast, the southwestern cavity is embedded in a region of slightly elevated temperature. If the large-scale surface brightness edges correspond to shock fronts, this region could mark the site where these shocks originated. Within the western extension of the 330 MHz radio source, T12a identified an arc of hotter gas separating the cavities inside the southwestern cavity at

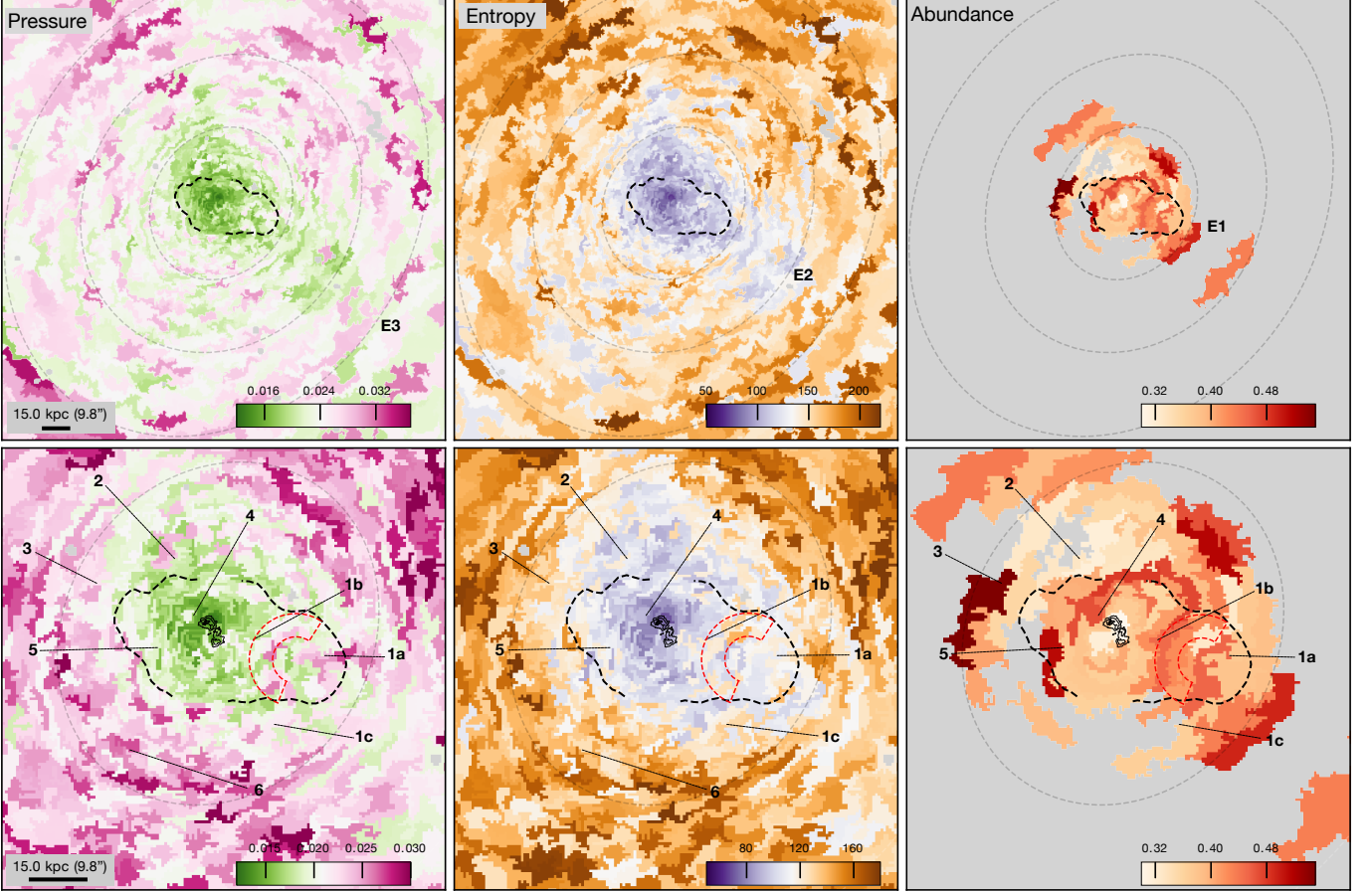


**Figure 7.** Pseudo-pressure (*left column*), entropy (*middle column*), and abundance (*right column*) maps of the ICM in Abell 2597. *Top row:* Large-scale 150 kpc x 250 kpc view of each map. Lower-pressure and lower-entropy gas coincide with the coolest regions. Metal enrichment is concentrated near the cluster core, with slightly higher abundances along the inner two surface brightness edges. *Bottom row:* Central 60 kpc view of each map. Higher-pressure and higher-entropy gas surround the region just outside the 330 MHz radio source as well as the hot arc. The most enriched gas is primarily aligned with the axis of the 330 MHz source.

$S/N \sim 30$ . We confirm the presence of this feature in our deeper data, marking it with dashed red lines.

Figure 7 presents the pseudo-pressure, entropy, and abundance maps of the ICM, with the top row displaying the large-scale structure. The pseudo-pressure and pseudo-entropy distributions closely follow the temperature map, with lower-pressure and lower-entropy gas coinciding with the coolest regions of the ICM. The abundance map, while more uncertain due to larger statistical errors, shows preferential enrichment along the radio-jet axis, and additional enrichment to the north. Across larger radii, we observe elevated pressure and entropy at the locations of the surface brightness edges, consistent with weak shocks or compressive heating. A similar trend is seen in the inner and middle edges of the abundance map, along the direction of the radio source.

Within the central 60 kpc (lower panels), the north-eastern filament base cavity contains gas at higher pressure and entropy than its surroundings. Although abundance

measurements in this region are less constrained, there is some indication that the gas inside the cavity is more metal-enriched than the gas outside of it. Similarly, the 330 MHz radio source is embedded in a region of elevated pressure and entropy, with the hot arc exhibiting particularly high values in both properties. The abundance of the gas surrounding the large radio source is enriched relative to the cluster mean ( $0.4Z_{\odot}$ ), with the highest enrichment observed in the region extending beyond the hot arc.

#### 3.4.1. 150 kpc - Scale Cocoon Shock?

Cocoon shocks form as the expanding plasma from the AGN compresses and displaces the ambient gas (Enßlin 2001), manifesting as surface brightness edges encircling the lobes. The shock edges are typically strongest in regions perpendicular to the jet axis, where the shock-driven compression is most pronounced (e.g., Randall et al. 2015; Snios et al. 2018). To determine whether

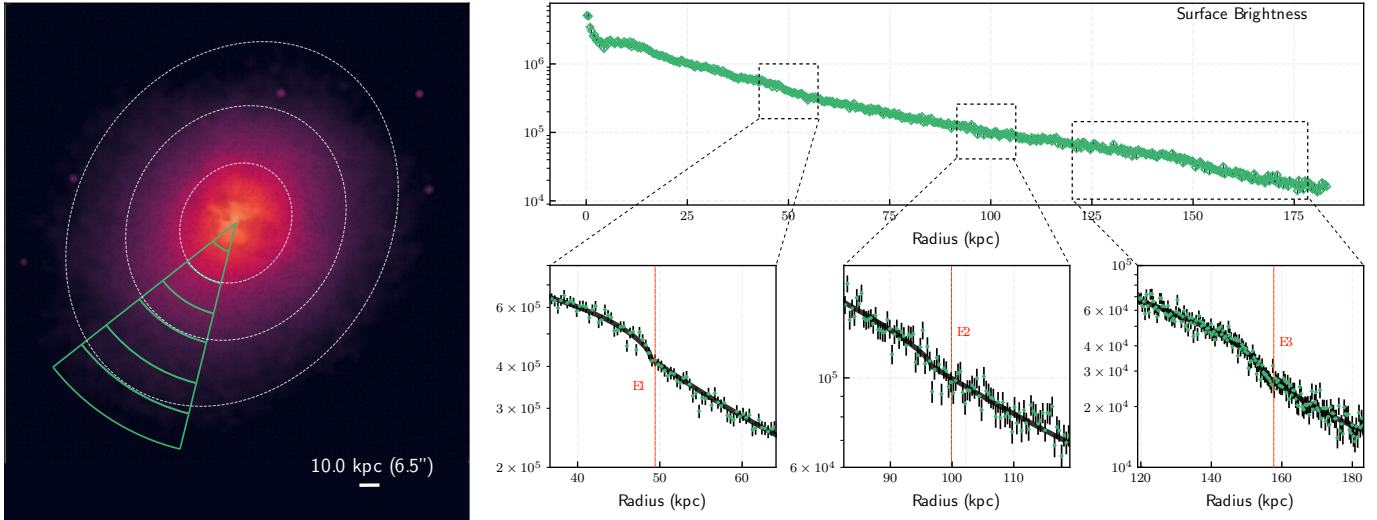


**Figure 8.** Surface brightness profiles for the southeastern sector of Abell 2597, where the surface brightness edges are most prominent. *Left:* *Chandra* X-ray image with green radial wedges indicating the regions used for spectral extraction. *Right:* Surface brightness profile across the entire wedge (*top*), showing clear discontinuities at each edge. The lower panels provide zoomed-in views of these edges, with fits performed using PYPROFFIT.

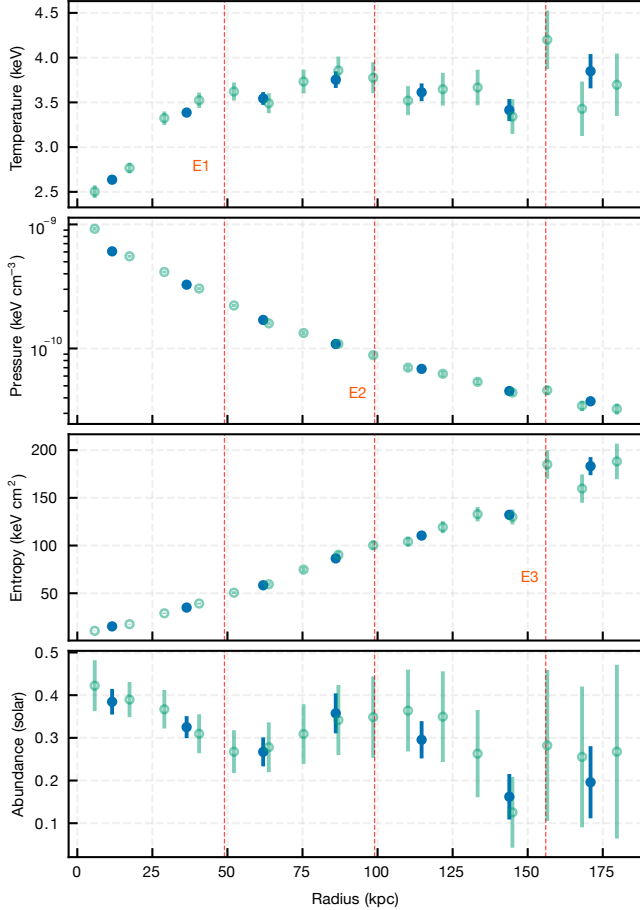


**Figure 9.** Spectral profiles across the surface brightness edges, with vertical dashed lines marking the breaks identified by PYPROFFIT. The mild temperature jumps observed across each edge suggest these features are weak shock fronts.

the surface brightness edges in the outer regions of the cluster correspond to shock discontinuities, we analyzed the surface brightness profile within the southeastern elliptical sector shown in the top left panel of Figure 8. We extracted the profile using  $0''.25$ -width radial annuli and fit the data with a broken power law using PYPROFFIT. The fitting confirmed surface brightness breaks at  $\sim 49$ ,  $99$ , and  $156$  kpc, with corresponding density jumps of  $1.17 \pm 0.03$ ,  $1.11 \pm 0.04$ , and  $1.23 \pm 0.05$ , respectively.

We examined the thermodynamic properties across each edge by extracting spectra from the wedges shown in Figure 8, with counts ranging from 5,000 to 25,000 per wedge. The top panel of Figure 9 shows the temperature profile, revealing  $1 - 2\sigma$  increases in the temperature at each edge (marked by vertical red dashed lines). Although subtle jumps are observed in the temperature profile, the corresponding pressure profile is less conclusive. At the outermost edge, we detect only a  $\sim 0.5\sigma$  pressure jump, making the discontinuity far less pronounced than suggested by the pseudo-pressure map. No clear pressure jumps are observed near the inner and middle edges, though subtle breaks in the profile are present. Additionally, the temperature jumps are not consistently located before each edge (e.g., Edge 1 and Edge 3), as would be expected in a well-defined shock front (Markevitch & Vikhlinin 2007). This raises the possibility that the observed discontinuities are cold fronts rather than shocks. However, interpreting them as cold fronts also presents challenges, which we explore further in Section 4.2.

For now, we interpret the edges as shock fronts and estimate their Mach numbers,  $\mathcal{M}$ , based on the fitted

Property	Edge 1	Edge 2	Edge 3
$D$	49 kpc	99 kpc	156 kpc
$\rho_2/\rho_1$	$1.17 \pm 0.03$	$1.11 \pm 0.04$	$1.21 \pm 0.05$
$T_2/T_1$	$1.10 \pm 0.08$	$1.12 \pm 0.10$	$1.25 \pm 0.20$
$\mathcal{M}$	$1.11 \pm 0.02$	$1.07 \pm 0.03$	$1.14 \pm 0.03$
$E_{\text{shock}}$	$3 \times 10^{58}$ erg	$5 \times 10^{58}$ erg	$1 \times 10^{59}$ erg

**Table 3.** Properties of the surface brightness edges in Abell 2597.  $D$  is the projected distance from the X-ray peak, measured at the density discontinuity in the surface brightness profile.

density jump, since it is detected at much higher significance than the pre-shock temperature and post-shock temperatures. Using the Rankine-Hugoniot relation for the density jump

$$\frac{\rho_2}{\rho_1} = \frac{(\gamma + 1)\mathcal{M}^2}{(\gamma - 1)\mathcal{M}^2 + 2}, \quad (1)$$

where  $\rho_2/\rho_1$  is the density ratio listed in Table 3.4.1, we obtain Mach numbers of  $1.11 \pm 0.02$ ,  $1.07 \pm 0.03$ , and  $1.14 \pm 0.03$  for the inner, middle, and outer edges, classifying each as very weak shock fronts.

Following Section 5.6 of Randall et al. (2010), we can estimate the total energy  $E$  imparted to the ICM from each shock as:

$$E \approx PV(f_P - 1), \quad (2)$$

where  $V$  is the gas volume contained within the shock front,  $P$  is the pressure across the front, and  $f_P = (P + \Delta P)/P$  describing the ratio of the post- and pre-shock pressure.

Since direct pressure jumps are not clearly detected for all shock fronts, we can relate  $f_P$  to the Mach number from the Rankine-Hugoniot shock jump conditions as

$$f_P = \frac{2\gamma\mathcal{M}^2 - (\gamma - 1)}{\gamma + 1}, \quad (3)$$

where  $\gamma = 5/3$  and the Mach number is taken from that estimated from the observed density and temperature jumps.

The pre-shock pressure for each ring is taken from the pressure closer to the central region from the extraction carried out in Figure 8. To calculate the volume of the gas enclosed by each shock front, we assume the depth of the front is the same as the length of the minor axis, and the width of each shock front is about  $1''.0$  ( $\sim 1.5$  kpc). By considering an ellipsoidal volume for the region enclosed by each shock front, we estimate the energy to be  $\sim 3 - 10 \times 10^{58}$  erg per front. Because we assume a constant Mach number over each shock's life, the energy calculated using this formula may slightly underestimate the total shock energy, as the Mach number likely would

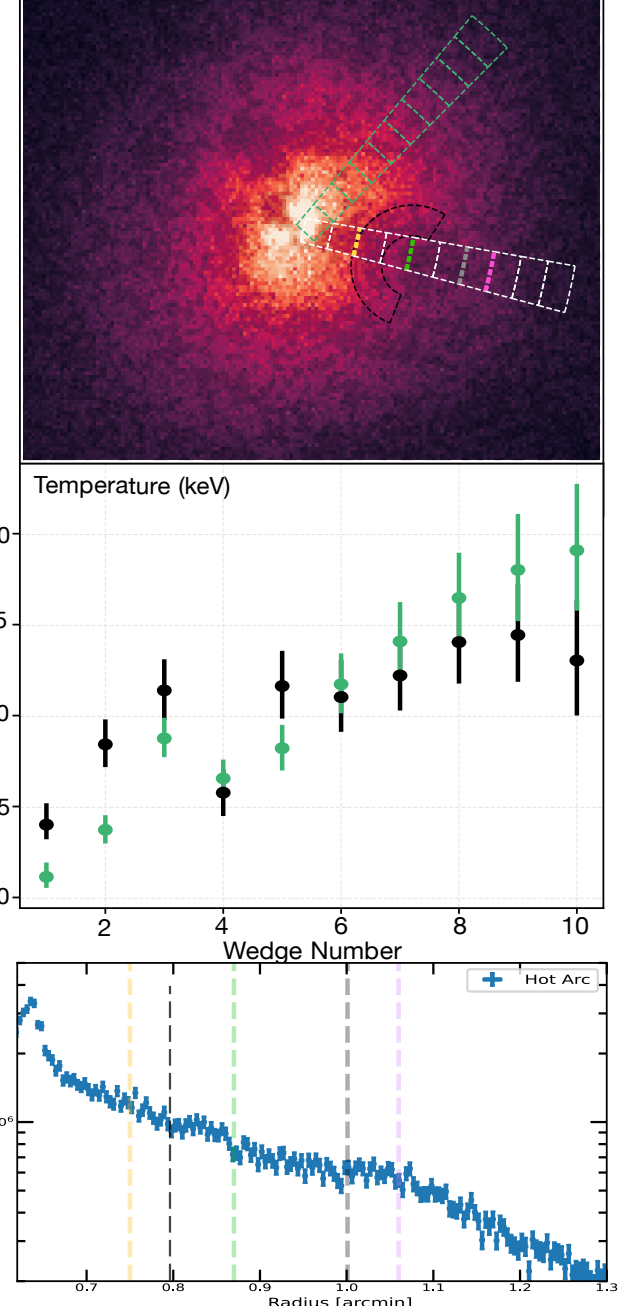


**Figure 10.** *placeholder* Top: Regions used for spectral extraction, with the hot arc outlined in white and a control region rotated  $\sim 45^\circ$  north in green. Bottom: Temperature profile for both regions, showing a  $\sim 1-2\sigma$  increase in the hot arc compared to the surrounding cluster gas.

have been higher during earlier stages of the shock's development. Nevertheless, the shock energy derived from this approach generally aligns within a factor of a few with estimates from hydrodynamical simulations of a central point explosion (e.g., Randall et al. 2010).

#### 3.4.2. Hot Arc Associated with Teardrop Cavity?

Although the spectral maps confirm the presence of the hot arc identified by T12a, assessing its statistical significance relative to the surrounding gas requires further spectral analysis, which our deep data now allow us to perform. In the top panel of Figure 10, we show the regions used for spectral extraction: the hot arc (outlined in white) and a control region rotated  $\sim 45$  degrees north (green), where fewer X-ray cavities are present. The lower panel displays the results of the spectral fitting.

The hot arc exhibits a localized temperature increase, exceeding the general cluster temperature trend in that region by  $\sim 1 - 2\sigma$ . Additionally, the temperature initially decreases before rising again, a pattern also observed in the temperature map, with deviations from the overall cluster profile reaching  $\sim 1 - 2\sigma$  significance. Given the consistency of these deviations, we conclude that the hot arc

when I extract a surface brightness profile throughout the arc (lower panel of figure 10, black line), there are clear discontinuities, with a jump of 1.42 ( $M \sim 1.28$ ) directly at the arc. Can we interpret it as a shock? The other cavities don't have profiles like this, but again, none of them are as big so... If it does correspond to a shock, the fraction of energy replaced by shock heating is around 1%.

### 3.5. X-Ray Cavities

To estimate the energetics of the cavities identified in Section 3.1, we estimate their buoyant rise times and the energy they dissipate as they ascend. The results, along with each cavity's effective radius—spherical or elliptical as appropriate—are summarized in Table 4.

Assuming each cavity formed near the X-ray peak, where the active radio source is located, and rose buoyantly to their current projected positions, we can estimate the cavity age as

$$t_{\text{cav}} = R/v, \quad (4)$$

where  $R$  is the projected distance from the ICM peak and  $v$  is the bubble's rise velocity. To estimate  $v$ , we consider two characteristic velocities: the sound speed  $c_s$ , which serves as an upper limit on gas motions within the ICM, and the terminal velocity  $v_t$ , which accounts for the impact of the ICM's ram pressure on the buoyancy force.

We estimate  $c_s$  using

$$c_s = \sqrt{\gamma kT / \mu m_p}, \quad (5)$$

where the adiabatic index for a monatomic gas  $\gamma = 5/3$ ,  $m_p$  is the proton mass, and the mean molecular weight

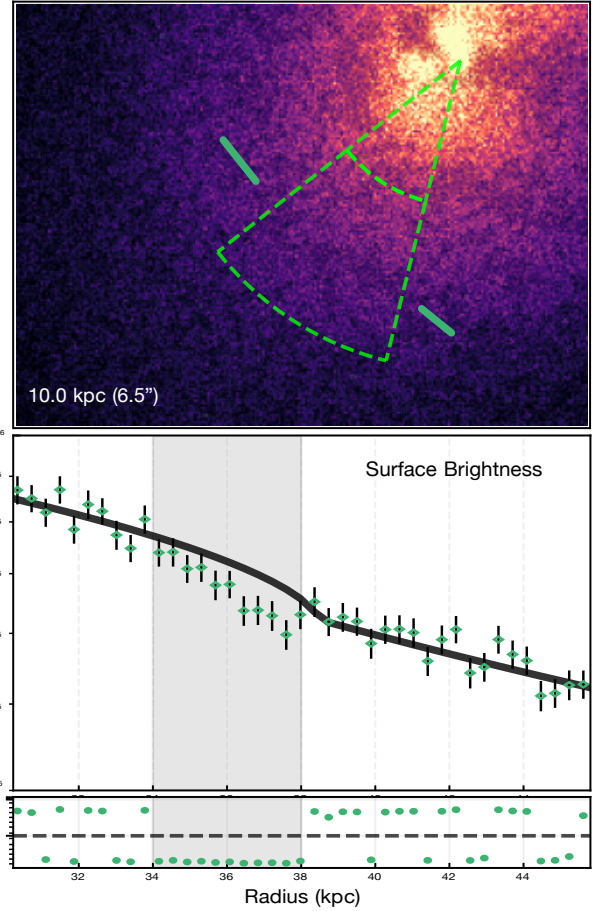


**Figure 11.** *Top:* Unfiltered X-ray image overlaid with a  $9.8'' - 0.98$  unsharp mask to enhance surface brightness depressions. The X-ray channel is marked with solid green lines, and finely spaced surface brightness profiles are extracted from the wedge outlined by dashed lines. *Bottom:* Surface brightness profile fitted with a broken power-law model assuming no deficit. The channel is detected at  $\sim 3\sigma$  below the model, indicating a  $\sim 10\%$  brightness deficit.

$\mu = 0.62$ . The terminal velocity is calculated following Churazov et al. (2001):

$$v_t = \sqrt{\frac{2gV}{SC}}, \quad (6)$$

where  $V$  is the bubble's volume,  $S$  is its cross-sectional area,  $C = 0.75$  is the drag coefficient, and  $g$  is the gravitational acceleration.

Each cavity is modeled as a sphere or ellipsoid, with the minor axis radius taken as the depth (see Table 4). Following Bîrzan et al. (2004), we calculate  $g$  using the stellar velocity dispersion of the BCG, under the approximation that the galaxy is an isothermal sphere:  $g \approx 2\sigma^2/R$ , where  $\sigma = 350 \text{ km s}^{-1}$  is the median stellar velocity dispersion across the BCG (see Figure 11 in Tremblay et al. (2018)) and  $R$  is the projected distance of the cavity from the center of the BCG.

Label	Cavity	$R(D)$ (kpc)	$r_{major}$ (kpc)	$r_{minor}$ (kpc)	$t_{buoy}$ (Myr)	$t_{cs}$ (Myr)	$pV$ ( $\times 10^{57}$ erg)	$P_{cav}$ ( $\times 10^{43}$ erg s $^{-1}$ )
(1)	(2)	(3)	(4)	(5)	(6)	(7)	(8)	(9)
1a & 1b	Total SW Ghost Cavity	22.0	16.6	7.2	40.3	26.8	47.8	18.1
1c	Broken off Piece of SW Ghost Cavity	27.8	22.1	5.8	63.3	33.8	35.3	9.2
2	NE Ghost Cavity	21.5	8.2	8.2	36.6	26.2	30.9	12.5
3	Outer NE Ghost Cavity	32.8	10.4	7.9	70.3	40.0	26.0	6.0
4	NE Filament Base Cavity	7.6	3.6	3.6	11.5	9.2	4.9	6.0
5	Eastern Ghost Cavity	16.3	6.9	4.6	32.2	19.9	9.9	4.8

**Table 4.** Properties of the X-ray Cavities in Abell 2597. Columns: (1) - (2) Cavity label and name given in Table 2; (3) Projected distance from the X-ray peak to the center of the cavity; (4) - (5) Major and minor radii; (6) Age assuming buoyant rise at terminal velocity; (7) Age assuming buoyant rise at the sound speed; (7)  $pV$  work done by inflation; (8) Cavity power, assuming relativistic plasma filling.[add the terminal velocity](#)

As cavities rise, they do work on the surrounding medium. We can estimate the cavity power,  $P_{cav}$ , as the ratio of the cavity enthalpy  $E_{cav}$  to its age  $t_{cav}$  as

$$P_{cav} = E_{cav}/t_{cav} = 4pV/t_{cav}, \quad (7)$$

where  $p$  is the ambient ICM pressure,  $V$  is the cavity volume, and  $t_{cav}$  is the average of the age estimates obtained from use of the terminal velocity vs. the sound speed.

Using the surrounding pressures reported in Table 4, we obtain cavity enthalpies ( $4pV$ ) ranging from  $\sim 2-20 \times 10^{58}$  erg. Employing the average age of each cavity derived from the buoyant rise time and synchrotron age estimates, we calculate cavity powers in the range of  $4-20 \times 10^{43}$  erg s $^{-1}$ . We discuss how this feedback counteracts the ongoing cooling flow in Abell 2597 further in Section 4.2.2.

### 3.6. The X-Ray Channel

The elongated X-ray “channel,” shown again in the top panel of Figure 11, runs roughly parallel to the southwestern radio jet, and is located a distance of  $\sim 35$  kpc to the southeast of the X-ray peak. The feature extends  $\sim 57$  kpc (37'') in length and  $\sim 8$  kpc (5'') in width. The lower panel of Figure 11 presents the surface brightness profile across the channel, revealing a  $\sim 3\sigma$  deviation from the expected profile if the feature represented a surface brightness break, modeled as a broken power law, rather than a true deficit.

Such channels are interpreted as thin sheets of lower-density gas within the ICM (Markevitch & Vikhlinin 2007). Assuming rough spherical symmetry for the main cluster body and a complete absence of gas within the 3D channel structure, the sheet’s extent along the line of sight would need to be [insert \(idk how to do this math. will ask maxim\)](#) kpc to produce the observed projected

X-ray brightness drop. However, since the channel cannot be entirely devoid of gas, its true extent is likely significantly greater. Similar subtle channels have been observed in the merging cluster Abell 520 (Wang et al. 2016) and the sloshing cool core of Abell 2142 (Wang & Markevitch 2018). We discuss the potential origin of this feature in Section 5.

## 4. HEATING THE RAPIDLY COOLING ICM

### 4.1. Thermal Instabilities and Residual Precipitation

In the classical picture of ICM cooling, thermal instabilities drive the condensation of colder, denser gas phases. As the ICM radiates energy, certain regions become unstable, leading to localized runaway cooling rather than uniform cooling across the cluster (McNamara & Nulsen 2012). This process is analogous to rain cloud formation on Earth, where water vapor condenses into droplets in regions of changing temperature and pressure.

As one of the most well-studied cool-core clusters across the electromagnetic spectrum, Abell 2597 provides a detailed view of cooling across all temperature phases, from the hot X-ray-emitting gas studied here to the coldest 100 K molecular gas detected with ALMA (Tremblay et al. 2016). The left panel of Figure 12 overlays these mapped phases as contours on the central X-ray map, showing that each phase follows the “S”-shaped structure seen in the core of the X-ray surface brightness distribution. This alignment supports the concept of a multiphase cooling cascade, where the hot X-ray bright gas progressively cools and condenses into progressively colder phases.

Several key timescales are predicted to govern the onset of thermal instabilities within the ICM. The free-fall time,  $t_{ff}$ , describes the time it takes for gas to collapse onto the central galaxy under its own gravity. In pure thermal instability models, when  $t_{cool}/t_{ff}$  falls below a

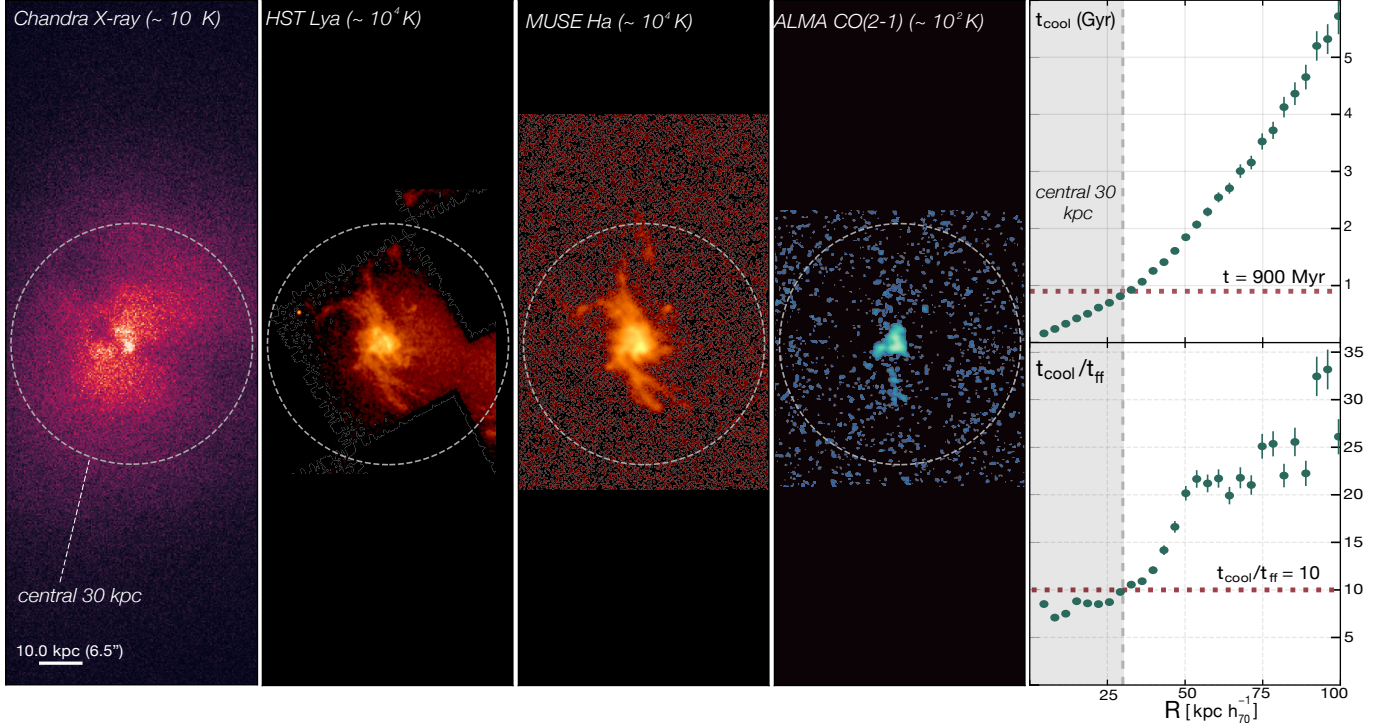


**Figure 12.** *Left four panels:* Multi-wavelength gallery from X-ray to sub-mm illustrating the multiphase gas within the central 30 kpc (dashed circle) of Abell 2597. *Right:* Radial timescales characterizing the thermodynamic state of the ICM, with the top panel showing the cooling time  $t_{\text{cool}}$ , and the lower panel displaying cooling-to-free-fall time ratio  $t_{\text{cool}}/t_{\text{ff}}$ .

critical threshold (in clusters around 10), local density fluctuations have time to precipitate and condense (Gaspari et al. 2012; McCourt et al. 2012; Sharma et al. 2012). The center panel of Figure 12 shows the radial profile of  $t_{\text{cool}}/t_{\text{ff}}$  in Abell 2597, revealing that the ratio falls below 10.

To quantify the cooling rate, the right panel of Figure 12 plots the cooling time  $t_{\text{cool}}$  as a function of the radius within the cluster. We estimated  $t_{\text{cool}}$  using

$$t_{\text{cool}}(r) \equiv \frac{3}{2} \frac{(n_e + n_p)kT(r)}{n_e n_H \Lambda(kT(r), Z)}, \quad (8)$$

where  $\Lambda$  is the cooling function (Sutherland & Dopita 1993). We evaluated  $\Lambda$  using an analytic fit Tozzi & Norman (2001) (Table 3), calibrated with coefficients describing gas with average metallicity  $Z = 0.3Z_{\odot}$ .

With  $r_{\text{cool}}$  defined as the radius where  $t_{\text{cool}} = 3$  Gyr (McDonald et al. 2018), the classical cooling rate within the central  $\sim 60$  kpc is  $\sim 210 \text{ M}_{\odot} \text{ yr}^{-1}$ . Observations, however, suggest significantly lower cooling rates. Using spectra from the *XMM-Newton* Reflection Grating Spectrometer, Fabian et al. (2023) estimated an X-ray cooling rate of  $\sim 67 \text{ M}_{\odot} \text{ yr}^{-1}$  after accounting for intrinsic absorption in the spectral fits, which captures soft X-ray emission hidden by photoelectrically absorbing cold clouds and dust near the centers of BCGs. This aligns with cooling rates inferred from O VI  $\lambda 1032$  ultraviolet

emission detected by FUSE, which, assuming the O VI  $\lambda 1032$  emission originates from thermal gas at  $\sim 7 \times 10^5$  K, suggests a cooling rate of  $\sim 40 \text{ M}_{\odot} \text{ yr}^{-1}$  within  $< 46$  kpc, or up to  $150^{+140}_{-100} \text{ M}_{\odot} \text{ yr}^{-1}$  when corrected for dust extinction (Oegerle et al. 2001).

Recent HST COS observations, which provide higher resolution UV data than FUSE, also detected the O VI  $\lambda 1032$  line, but within the central 2 kpc of the cluster (Vaddi et al., in prep). From the line's luminosity, Vaddi et al., in prep estimate a cooling rate of  $15.6 \pm 0.9 \text{ M}_{\odot} \text{ yr}^{-1}$  within the nuclear region. Assuming this rate holds roughly consistent out to  $\sim 30$  kpc, where ALMA derived a cold gas mass of  $3.2 \pm 0.1 \times 10^9 M_{\odot}$  (Tremblay et al. 2016, 2018), the residual cooling flow could fill the  $3 \times 10^9 M_{\odot}$  gas reservoir within the estimated 190 Myr cooling time at that radius, suggesting ongoing replenishment of the cold gas could be consistently replenished by the ongoing residual cooling flow.

## 4.2. AGN Feedback History and Power

### 4.2.1. Multiple Outbursts or Continuous Bubbling?

The most obvious candidate for reducing the  $\sim 210 \text{ M}_{\odot} \text{ yr}^{-1}$  cooling flow to the moderate  $\sim 15 \text{ M}_{\odot} \text{ yr}^{-1}$  cooling rate is AGN feedback. Abell 2597 is particularly notable for hosting an extensive network of ghost cavities, a phenomenon rarely observed in such abundance in nearby clusters. Previous analysis of these cavities

by T12a suggested they might originate from an AGN that alternates between active and quiescent phases or transitions between high and low activity modes. The estimated cycling time for these periods, on the order of  $10^7$  to  $10^8$  years, aligns with findings from other studies on the AGN duty cycle (see Figure 15 in Vantyghem et al. 2014).

However, the nature of this feedback—whether episodic or continuous—remains uncertain. Given that the oldest cavity has a buoyant rise time of  $\sim 1 \times 10^8$  years, C05 suggested that none of the observed cavities may be true “ghost” cavities but rather products of an ongoing AGN feedback episode. Determining whether the radio plasma filling the cavities originates from distinct outbursts or a single sustained event requires tracing spectral age gradients, but the limited frequency coverage and sensitivity of past radio observations and the archival GMRT data presented in this work have made this infeasible.

An alternative approach to constrain the timing between each episode of AGN feedback is to estimate the ages of the surface brightness edges observed in Figure 2. During an AGN outburst, jets not only inflate cavities but also drive weak shocks through the ICM.<sup>3</sup> If each edge represents a shock front from a separate AGN outburst, the time required for the shocks to reach their current positions ( $r_{\text{sh}}$ ) can be estimated using their Mach numbers from Section 3.4.1 with:

$$t_{\text{age}} = \frac{r_{\text{sh}}}{M c_s}, \quad (9)$$

where  $c_s$  is the sound speed of the undisturbed gas ahead of the shock, determined using the temperature outside the shock front. It’s important to note that this approach may slightly overestimate the actual age of the shock by about 10–20% (as noted by Russell et al. (2010)), since the shocks likely started with higher Mach numbers when first launched. Furthermore, the shocks are elliptical and slightly asymmetric, meaning their evolution may vary across different regions of the ICM, introducing additional uncertainty in age estimates.

Applying this approach, we estimate the ages of the shock fronts to be approximately 50 Myr for the inner shock, 80 Myr for the middle shock, and 100 Myr for the outer shock. The outer shock’s age, around  $1 \times 10^8$  years, aligns with the estimated age of the oldest radio source, suggesting that the expansion of the oldest

<sup>3</sup> Of course, AGN can also produce ultrafast outflows that inject energy into the surrounding gas without generating significant radio emission. These high-velocity winds, observed in X-ray and optical absorption lines, can carve out low-density cavities similar to those formed by relativistic jets.

radio lobe could have produced it. If the inner shocks are due to later outbursts from the radio source, their ages imply an average cycle time of  $\sim 2 \times 10^7$  years in between outbursts, consistent with findings from other cool-core systems with multiple rounds of AGN feedback (Vantyghem et al. 2014).

However, as discussed earlier, the nature of these edges remains uncertain. While the data favors their interpretation as shock fronts, the possibility that they are cold fronts cannot be ruled out, though it presents significant challenges. Cold fronts typically arise from contact discontinuities where cooler, denser gas moves through a hotter medium, making the presence of multiple concentric cold fronts difficult to explain. Typically, cold fronts show a sharp density discontinuity in one direction (see Markevitch & Vikhlinin (2007) for a review) and do not extend uniformly around the center of the cluster unless the motion of the gas is predominantly along our line of sight. In contrast, the nearly circular geometry of the observed fronts is naturally explained by an expanding cocoon of radio plasma, where the AGN outburst drives shocks into the ICM.

If the edges are indeed shock fronts, this supports the scenario of episodic AGN feedback, where multiple outbursts inflate cavities and drive shocks at intervals of  $\sim 10^7$ – $10^8$  years. However, it remains possible that all the observed cavities were produced during a single, prolonged AGN outburst rather than through discrete jet episodes separated by millions of years. In this scenario, the AGN would not undergo complete on-off cycles but instead exhibit continuous activity with variability in its accretion rate (i.e., “flickering” Schawinski et al. 2015). Like an aerator in a fish tank, the AGN would steadily inject energy into the surrounding medium, inflating bubbles in different directions over time (Fabian 2012). Initially, these cavities would expand rapidly, driving shocks outward, but as the energy input rate declines, the expansion slows, allowing the shocks to detach from the cavities and propagate into the ICM (Randall et al. 2015). If this is the case in Abell 2597, the observed cavities and weak shock features may reflect a more gradual and sustained AGN-driven “bubbling” process rather than episodic, large-scale jet eruptions with long quiescent phases.

#### 4.2.2. Inefficient Heating

Regardless of whether the AGN activity is episodic or continuous, the injected energy is more than sufficient to counteract radiative cooling. At an average cluster temperature of 3.5 keV and cooling radius of  $r \sim 60$  kpc, the total cooling luminosity  $L_{\text{cool}} \approx 2 \times 10^{44}$  erg s<sup>-1</sup> matches the total power output of the expanding

X-ray cavities,  $P_{\text{cav}} \sim 2 \times 10^{44} \text{ erg s}^{-1}$  (see Table 4). This balance, first noted in T12a and confirmed here, suggests AGN feedback regulates cooling in the cluster core, consistent with trends in nearly all other nearby cool-core clusters, with Abell 2597 fitting neatly along the  $P_{\text{cav}} - L_{\text{cool}}$  relation from Hlavacek-Larrondo et al. (2015) (see Figure 13).

While the correlation between cavity power and cooling luminosity is well-established, the exact mechanism by which energy from the cavities heats the ICM remains elusive. The detection of a “hot arc” bordering the inner edge of the largest X-ray cavity may support the idea of reading Any comments on the different spectral properties of the cavities feat 4 vs feat 1? I think feat 4 is the classic picture of bubbles dredging up low entropy gas, while feature 1 shows potential shock heating surrounding the cavity (via compression or sound waves?). or am i looking into it too much

The energy released during an AGN outburst is divided between the internal energy stored in the cavities and the work done by the cavities as they expand, which in turn drives the shock. Using the values listed in Table 3.4.1, we estimate a total shock energy on the order of  $\sim 4 \times 10^{59} \text{ erg}$ , with the total cavity enthalpy contributing approximately 40% of this total.

From the shock ages derived in Section 4.2.2, we estimate shock powers of  $1.9 - 3.2 \times 10^{43} \text{ erg s}^{-1}$ , about an order of magnitude lower than the cooling luminosity at each shock’s radius. Although the total power from shocks is  $\sim 10^{44} \text{ erg s}^{-1}$ , it remains insufficient to fully quench the cooling flow. If the combined energy from shocks and cavities were entirely converted into heating, it could, in principle, offset all radiative losses and suppress cooling. However, several factors make this scenario unlikely.

First, weak shocks typically deposit only a small fraction of their energy, e.g. 5% in NGC 5813 (Randall et al. 2010), as heat within the cooling radius. In Abell 2597, we detect a  $\sim 3\sigma$  entropy increase only at the outer shock front. Following Randall et al. (2010), we estimate the energy injected by the shock that directly increased the entropy of the ICM using  $\Delta Q \simeq T\Delta S$ . For weak shocks, the entropy increase  $\Delta S$  corresponds to a fractional heat input relative to the gas thermal energy, given by  $\frac{\Delta Q}{E} \sim \Delta \ln(P/\rho^\gamma)$ , where  $E$  is the thermal energy and  $\gamma$  is the adiabatic index.

For the  $\sim 150$  kpc shock in A2597, we estimate the pressure jump across each shock using the Rankine-Hugoniot relation:

$$\frac{P_2}{P_1} = 1 + \frac{2\gamma}{\gamma+1}(\mathcal{M}^2 - 1), \quad (10)$$

where  $\gamma = 5/3$ . Using the values in Table 3.4.1, we find that shock heating replaces  $< 1\%$  of the local thermal energy of the gas at the shock front, making shock heating alone insufficient to counteract radiative cooling across the cluster. This result is consistent with the broader argument that while bubble enthalpy, weak shocks, and turbulent dissipation contribute to heating the ICM, they do not completely suppress cooling, as evidenced by the persistence of multiphase gas cospatial with the coldest X-ray bright gas.

### 4.3. SMBH Fuel Supply

The coexistence of hot, warm, and cold gas phases in the core of A2597 naturally raises the question: which phase primarily fuels its SMBH? Given the sustained AGN activity, a major and recurring fuel supply is necessary to maintain its power output. At the scale of the Bondi radius, where the SMBH’s gravitational influence dominates over thermal gas motions, fueling mechanisms are generally classified into two categories: hot fueling and cold fueling.

Hot fueling typically refers to Bondi accretion (Bondi 1952), where  $\sim 1$  keV gas is directly accreted onto the SMBH. To estimate an upper limit on the Bondi accretion rate within 760 pc, the native *Chandra* resolution, we use Equation 6 from Rafferty et al. (2006), which relates the accretion rate to the electron density  $n_e$ , gas temperature  $T$ , and black hole mass  $M_{\text{BH}}$  as:

$$\dot{M}_B = 0.012 \left( \frac{T}{\text{keV}} \right)^{-3/2} \left( \frac{n_e}{\text{cm}^{-3}} \right) \left( \frac{M_{\text{BH}}}{10^9 M_\odot} \right)^2 \text{M}_\odot \text{yr}^{-1}. \quad (11)$$

To update the black hole mass estimate from T12b, we use the spatially resolved MUSE data presented in Tremblay et al. (2018) to adopt a stellar velocity dispersion of  $\sim 290 \text{ km s}^{-1}$  within the nucleus. Using the  $M_{\text{BH}} - \sigma$  relation from McConnell et al. (2011) for elliptical galaxies, we calculate  $M_{\text{BH}} = 1.3 \times 10^9 M_\odot$ , giving a Bondi radius of  $\sim 22$  pc.

Since *Chandra* cannot resolve the Bondi radius  $r_B$  in A2597, we extrapolate  $n_e$  and  $T$  down to  $r_B$  using a beta model for the density profile (Russell et al. 2013b) and assume the temperature at the Bondi radius is approximately one-fourth of the central temperature from Table 3. Using  $n_e = 0.11 \text{ cm}^{-3}$ , we estimate the Bondi accretion rate at 760 pc to be  $\dot{M}_{B,760\text{pc}} \sim 5.3 \times 10^{-3} M_\odot \text{ yr}^{-1}$ . The Eddington accretion rate, calculated using Equation 5 in Rafferty et al. (2006) and  $\epsilon = 0.1$ , results in an accretion rate of  $\sim 30 M_\odot \text{yr}^{-1}$ . Both the Bondi and cavity-power-derived accretion rates are sub-Eddington, consistent with T12b.

To explore the implications for AGN fueling, we calculate the Bondi power as  $P_{\text{Bondi}} = \eta \dot{M}_{\text{Bondi}} c^2$ , where

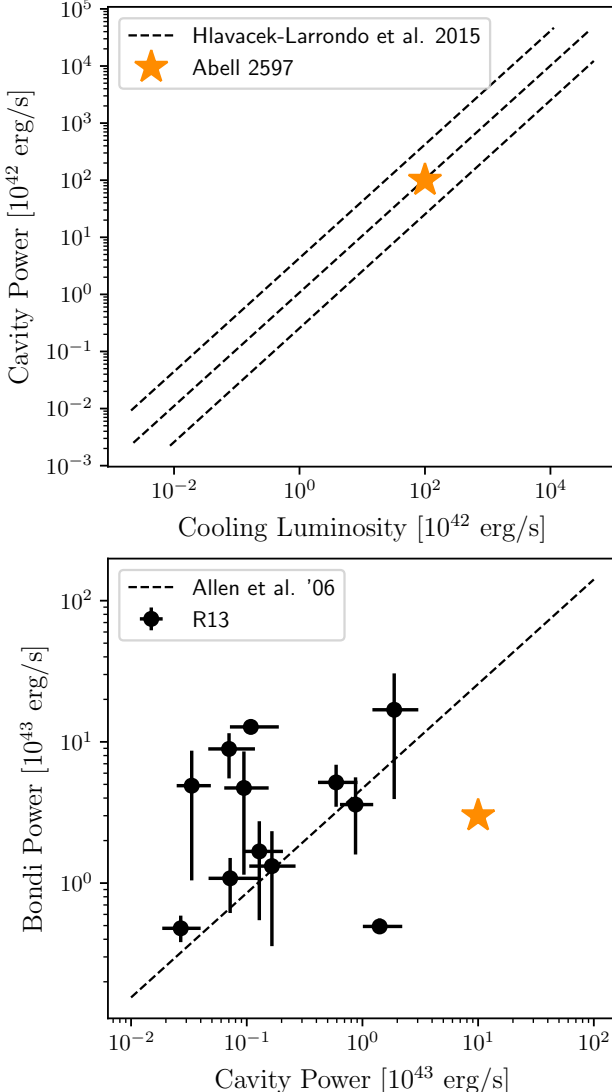


**Figure 13.** *Top:* Cavity power vs. cooling luminosity for Abell 2597 (orange star), plotted alongside the best-fit relation from Hlavacek-Larrondo et al. (2015) (dashed lines). Abell 2597 follows the typical trend where AGN cavity power scales with the radiative cooling luminosity of the ICM. *Bottom:* Cavity power vs. Bondi power, adapted from Russell et al. (2013b) and Allen et al. (2006). The Bondi power for Abell 2597 is significantly lower than the observed cavity power, suggesting Bondi accretion is not the dominant fueling mechanism.

$\eta = 0.1$  represents the radiative efficiency. Using our estimate for the Bondi accretion rate, this yields  $P_{\text{Bondi}} \sim 3 \times 10^{43} \text{ erg s}^{-1}$ . The lower panel of Figure 13 compares the Bondi power to the cavity power for A2597, along with data from Russell et al. (2013b). In A2597, the Bondi power falls an order of magnitude below the estimated cavity power, suggesting that hot mode accretion alone may not provide sufficient fuel to power

the observed AGN activity. This result is consistent with the findings for M87, where *Chandra* resolves the Bondi radius, yet the Bondi power is two orders of magnitude below the jet mechanical power (Russell et al. 2015; Bambic et al. 2023). In both clusters, assuming a lower mechanical efficiency of  $\eta \sim 10^{-2} - 10^{-3}$ , as suggested by simulations (e.g., Sadowski & Gaspari 2017), would further reduce the Bondi power by a factor of 10–100, making it an even less viable fueling mechanism for the AGN.

Early studies of nearby elliptical galaxies (e.g., Allen et al. 2006), reported a correlation between Bondi accretion power and AGN jet power, inferred from the enthalpy of jet-blown cavities. However, this correlation is subject to significant uncertainties, including projection effects and assumptions about subsonic cavity inflation. A subsequent analysis by Russell et al. (2013b) using a larger sample found a weaker correlation, further emphasizing that Bondi accretion alone cannot fully explain the observed AGN power. In A2597, as in other systems, additional fueling mechanisms, such as cold/chaotic accretion, seems to be required to bridge the gap between the hot-mode power and the observed energy output (and imprints) of the AGN.

In the cold fueling channel, thermally unstable gas cools and condenses out of the hot ICM, forming dense clouds and filaments. In Chaotic Cold Accretion (CCA) theory (Gaspari et al. 2013, 2018), thermal instability is indicated by the condensation ratio  $C \equiv t_{\text{cool}}/t_{\text{eddy}}$ , where  $t_{\text{eddy}}$  is the eddy turnover time and given by:

$$t_{\text{eddy}} = 2\pi \frac{r^{2/3} L^{1/3}}{\sigma_{v,L}}, \quad (12)$$

where  $L$  is the turbulence injection scale and  $\sigma_{v,L}$  is the gas velocity dispersion.

Since turbulence in the ICM is difficult to measure directly, we estimate the ICM's velocity dispersion using two independent tracers. As a lower limit, we adopt the velocity dispersion of the CO filament,  $\sigma_{\text{mol,1D}}$ , which has a median line-of-sight value of  $\sim 50 \text{ km s}^{-1}$  (Tremblay et al. 2018). Correcting for three-dimensional motion, we obtain  $\sigma_{\text{mol}} \approx 87 \text{ km s}^{-1}$ . For an upper limit on the ICM velocity dispersion, we take the  $\sim 480 \pm 120 \text{ km s}^{-1}$  estimate from Table 4 of Sanders & Fabian (2013), which derived the velocity width of the cool X-ray emitting gas from *XMM-Newton* RGS spectral broadening and *Chandra* surface brightness fluctuations. Following previous studies (e.g., Gaspari et al. 2018; Juráňová et al. 2019; Olivares et al. 2022; Temi et al. 2022), we estimate the injection length scale  $L$  using the extent of the filamentary gas. Based on the H $\alpha$  contours in Figure 12, we adopt  $L \sim 30 \text{ kpc}$ , which

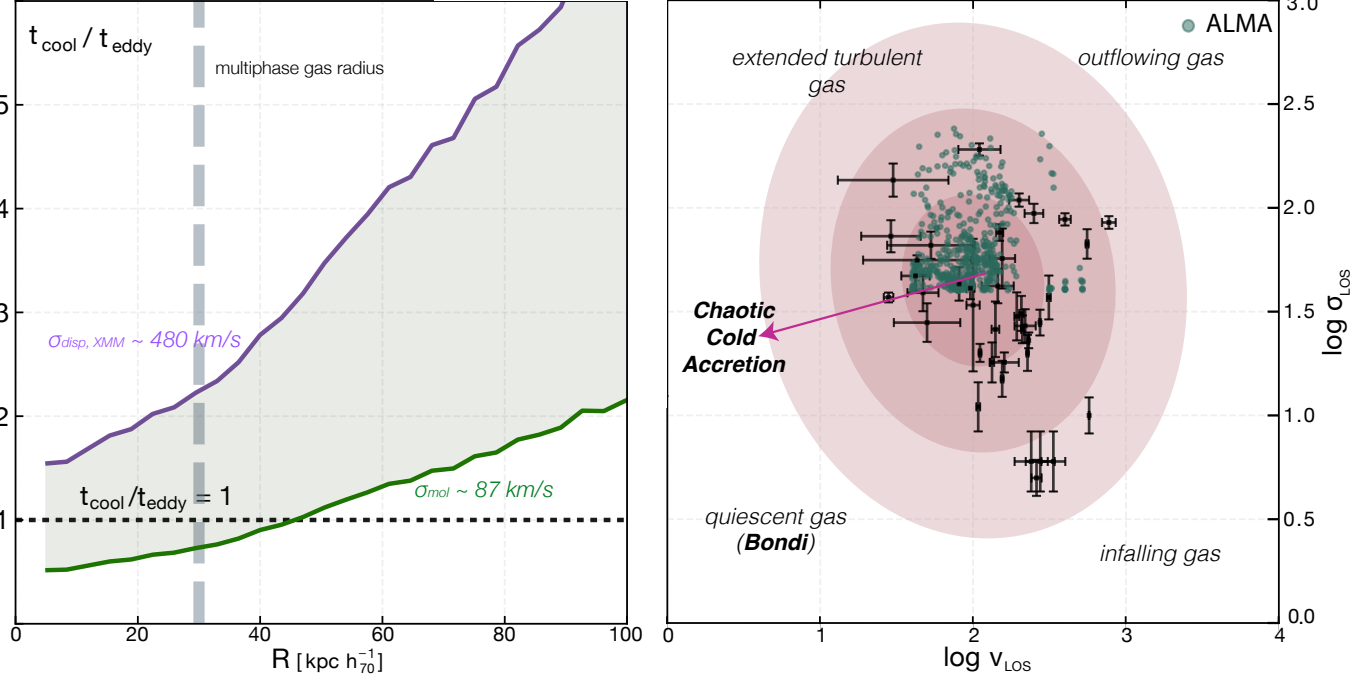


**Figure 14.** *Left:* Condensation-ratio ( $C \equiv t_{\text{cool}}/t_{\text{eddy}}$ ) in A2597, with colors indicating different velocity dispersions used to estimate  $t_{\text{eddy}}$ . The vertical dashed line marks the central 30 kpc, where cooler multiphase gas exists, while the horizontal dotted line indicates  $t_{\text{cool}}/t_{\text{eddy}} = 1$ , below which turbulent thermal instabilities are expected. *Right:* k-plot showing the kinematics of cold gas traced by archival ALMA CO(2-1) data (Tremblay et al. 2018), with velocity dispersion on the y-axis and line-of-sight velocity on the x-axis. Cold-phase points (green) represent individual spatially resolved measurements and align with the 1–3 $\sigma$  contours of CCA simulations (Gaspari et al. 2018). Black points show median kinematics for gas in entire massive galaxies rather than individual spaxels, including A2597 nuclear absorption features (bottom-right points). A2597’s cold-phase concentration in the central raining zone favors cold fueling (CCA) over hot fueling (Bondi accretion).

is nicely consistent with the  $\sim 22$  kpc average bubble diameter (see Table 4).

The left panel of Figure 14 shows the condensation ratio falling below unity within the central 30 kpc when using  $\sigma_{\text{mol}}$  and ranging between  $C \sim 1 – 2$  with  $\sigma_{\text{XMM}}$ . These results suggest that turbulence-driven thermal instability allows the ICM to cool rapidly over tens of kpc. If the resulting cold structures lose or maintain low angular momentum through inelastic collisions, they can accrete onto the SMBH at rates exceeding those of Bondi accretion alone (Pizzolato & Soker 2005; Gaspari et al. 2015).

CCA predicts that turbulence enhances cold gas accretion, leading to intermittent bursts in SMBH fueling up to two orders of magnitude above the Bondi rate (Gaspari et al. 2017). To better assess the kinematics of the cold gas in A2597, the right panel of Figure 14 presents the pencil-beam kinematical plot (k-plot) diagnostic from Gaspari et al. (2018), where “pencil-beam” refers to small-aperture (less than a few arcseconds) observations that resolve localized gas kinematics. The plot shows the relationship between velocity dispersion  $\sigma_{\text{los}}$  (tracing turbulence) and line-of-sight velocity shifts

$v_{\text{LOS}}$  (tracing bulk motions) in the multiphase gas, with previously published values from massive galaxies (black points) and ALMA-detected clouds in A2597 (green circles). The cold clouds in A2597 closely follow CCA predictions, with most falling within the 1 $\sigma$  contours of high-resolution CCA simulations.

While the center of the k-plot defines the strong “raining” region, the four outer quadrants trace other potential regimes at play (see labels in Figure 14). We observe several clouds drifting in the macro-scale weather (high turbulence, but low shifts) and a few in the opposite regime with high bulk velocities and very narrow lines, which are often tied to the infalling clouds toward the nuclear region. The black points in the bottom-right quadrant are ALMA absorption features (against the radio AGN continuum) detected in A2597 (Tremblay et al. 2016), interpreted as “shadows” cast by the infalling clouds. These massive ( $\sim 10^5 – 10^6 M_{\odot}$ ) clouds could supply an accretion rate of  $\sim 0.1$  to a few  $M_{\odot}\text{yr}^{-1}$  if they are indeed falling directly towards the SMBH; the ultimate feeding rate would depend on the efficiency of angular momentum loss mechanisms (e.g., inelastic collisions and effective viscosity; Gaspari et al. 2017).

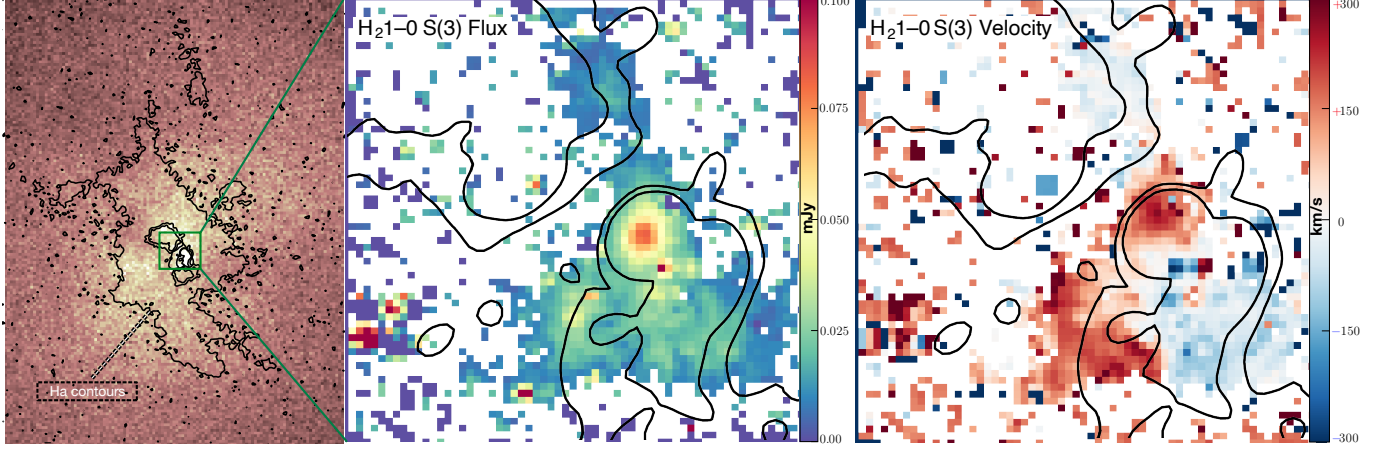


**Figure 15.** Distribution and kinematics of the multiphase gas in the core of A2597. *Left two panels:* *Chandra* X-ray map with black  $\text{H}\alpha$  contours, showing warm gas draped around the rims of the southwestern cavity and northern ghost cavities. The dashed green square marks the region shown in the new SINFONI AO maps. *Right two panels:* The SINFONI  $\text{H}_2$  (1-0)  $\text{S}(3)$  flux map (middle right) shows molecular gas aligned with the edges of the northern and southern radio lobes of the 8.4 GHz radio source (black contours). The velocity map (right) shows molecular gas kinematics influenced by interactions with the radio lobes.

Conversely, the strong outflowing (top-right) and quiescent accretion quadrants (bottom-left) are not significantly filled in A2597, again consistent with the above findings that hot-mode feeding is secondary, and that A2597 does not drive ultrafast outflows (e.g., Laha et al. 2021). Observations of A2597 (and several other systems; e.g., Olivares et al. 2022, 2025; Temi et al. 2022), including CO absorption lines tracing molecular gas inflow (Rose et al. 2023), further support this ‘raining’ picture.

In future work, we will present the deep *Chandra* data alongside new JWST MIRI and NIRSPEC observations of the nucleus of A2597. This will allow us to better constrain the gas mass budget and kinematics within the Bondi/BH influence radius, and better determine the relative contributions of cold and hot gas to the feeding process within meso-micro scales.

#### 4.4. The Multiphase Fountain

##### 4.4.1. Stimulated Uplift

Although the residual cooling rate is sufficient to supply the entire cold gas mass reservoir, it is clear that multiple rounds of AGN feedback have significantly shaped the distribution of this gas, as noted in Section 4.2 of (Tremblay et al. 2018). The left panel of Figure 15 shows that the warm gas traced by  $\text{H}\alpha$  is cospatial with the outer X-ray cavities, draping around the rims of the southwestern teardrop-shaped cavity, as well as the northern ghost cavities. In the nuclear region, the right panel of Figure 15 shows the warm molecular gas probed by the vibrational  $\text{H}_2$  (1-0) transition is similarly draped around the edges of both the northern and southern lobes of the 8.4 GHz radio source, suggesting

that the radio lobes are dynamically shaping the inner gas reservoir. The spatial correlation between the multiphase gas and the cavities implies two possibilities: (1) the gas has been entrained and uplifted by the jetted outflows, and/or (2) it has formed *in situ* from cooling warm outflows.

Tremblay et al. (2018) primarily explored the first scenario, where pre-existing cold gas is uplifted by buoyant X-ray cavities. They demonstrated that the mechanical energy of the cavity network is sufficient to lift the entire cold molecular nebula, as the displaced hot gas mass exceeds the cold gas mass, making uplift energetically feasible based on Archimedes’ principle. Further supporting this scenario is the apparent alignment of the cold gas with the X-ray cavities in projection and the bulk velocities of the  $\text{H}\alpha$  filaments ( $\sim 375 \text{ km s}^{-1}$ ), which are consistent with the terminal velocity of the rising bubbles (see Table 4). However, this alignment is only observed in projection, and without velocity measurements of the hot gas, it remains uncertain whether the cold gas is physically co-moving with the bubbles or simply coincident along our viewing angle. Future XRISM observations will be crucial in resolving this question, particularly since the kinematics of the extended multiphase nebula in Abell 2597 are mapped in far greater detail than in other cool-core clusters like Perseus and M87.

Alternatively, some hydrodynamical simulations suggest that AGN outflows can trigger in-situ cooling, where filament velocities are primarily governed by bulk bubble motions rather than turbulence (e.g., Qiu et al. 2020; Zhang et al. 2022). Since the buoyant rise time

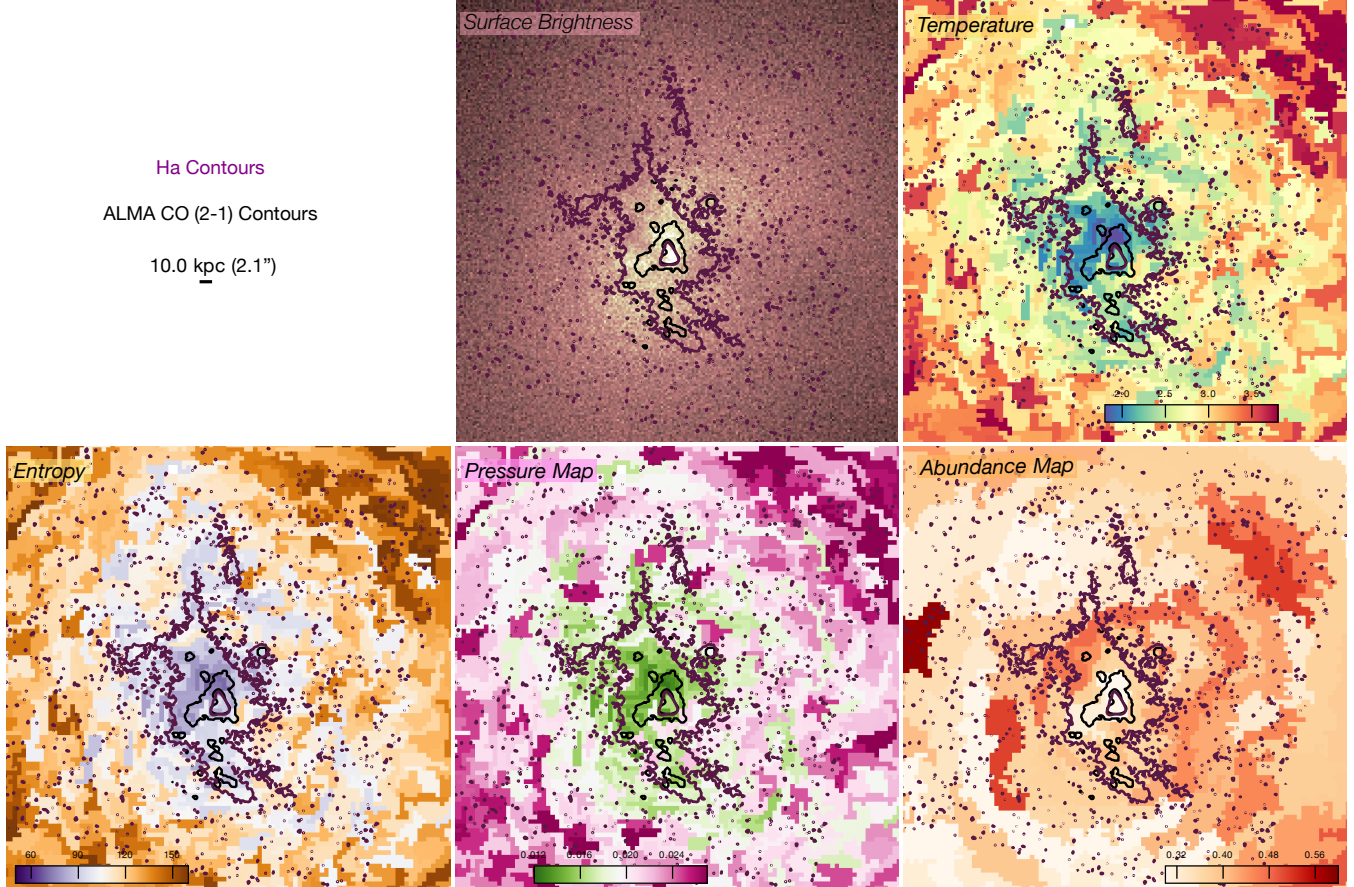


**Figure 16.** will clean contours Spectral maps of the multiphase fountain in A2597 with  $\text{H}\alpha$  (purple contours) and CO(2-1) (black contours) overlaid, showing the relationship between X-ray-emitting hot gas and cooler phases. Cooler X-ray gas aligns with the multiphase filaments, suggesting ongoing radiative cooling, while localized regions of elevated temperature, entropy, and pressure appear near the northern cavities and along the filament bordering the southwestern cavity. These regions are more metal-enriched than the very center, consistent with AGN-driven outflows uplifting enriched material from the galaxy.

of the bubbles ( $\sim 10^8$  yr) is comparable to the cooling time within the region where cold filaments are observed, some fraction of the cold gas may have condensed from the warm phase while being uplifted. However, the k-plot in Figure 14 shows no strong bulk motions in the cold gas, suggesting that compressional condensation through outflows plays a secondary role compared to global condensation driven by the ICM weather.

#### 4.4.2. Spectral Properties

We present detailed surface brightness and spectral maps of the multiphase fountain in Figure 16, showing the relationship between the X-ray-emitting hot gas and the cooler phases traced by  $\text{H}\alpha$  (purple contours) and CO(2-1) (black contours) in projection.

The top middle panel shows the relationship between the multiphase gas and the X-ray surface brightness distribution, with all phases clearly cospatial in projection. A recent study by Olivares et al. (2025) found a strong correlation between the X-ray and  $\text{H}\alpha$  surface

brightness of filaments across multiple clusters, suggesting a direct connection between the hot and warm gas phases. In Abell 2597, the X-ray to  $\text{H}\alpha$  surface brightness ratio remains nearly constant at around 3, slightly below the sample average of 4, regardless of the distance to the AGN. This consistency indicates that local processes—such as turbulent mixing layers, shocks, or reprocessing of extreme ultraviolet and X-ray radiation from the cooling ICM—play a dominant role in regulating the excitation of the filaments rather than AGN proximity alone. These results are also consistent with predictions from CCA models, which our analysis of cold filaments in Section 4.3 independently support.

Spectrally, the X-ray gas in regions cospatial with the multiphase filaments is notably cool, consistent with ongoing radiative cooling. However, localized temperature enhancements are observed north of the  $\text{H}\alpha$  filament near the northern ghost cavities and to the south along the filament bordering the southwestern ghost cavity. The entropy and pressure maps exhibit a similar pat-

tern, with elevated temperature regions also showing slightly higher entropy and pressure, likely indicating AGN feedback modifying the thermodynamic state of the uplifted gas.

The abundance map, though more uncertain, suggests that the X-ray gas within the filaments is less metal-enriched than the surrounding gas. The outward displacement of these metal-rich regions is consistent with enrichment driven by the expansion of AGN-inflated cavities. The large scale abundance emap in Figure 7 shows that the metal enriched region are mostly along the direction of the 330 MHz source, supporting the idea that AGN feedback redistributes metals into the surrounding ICM (Kirkpatrick et al. 2009; Simionescu et al. 2009).

We emphasize that all these correlations are observed in projection, and the true three-dimensional distribution of the gas remains uncertain. Structures that appear aligned in projection may not be physically connected, affecting the apparent correlation between filaments and cavities and the spectral features of the gas surrounding the cavities.

## 5. THE ORIGIN OF THE X-RAY CHANNEL

The elongated X-ray surface brightness “channel” identified in Figure 2 is likely a thin sheet of lower-density gas. Similar channels have also been observed in other systems, such as the merging cluster Abell 520 and the sloshing cool core of Abell 2142 (Wang et al. 2016; Wang & Markevitch 2018). While such structures might theoretically result from two opposing cold fronts, this scenario is unlikely for A2597, as it was for A520 and A2142. Instead, these features are more plausibly interpreted as plasma depletion layers (PDLs), a phenomenon observed near planets (e.g., Øieroset et al. 2004) and reproduced in magnetohydrodynamic (MHD) simulations of galaxy clusters (ZuHone et al. 2011). In the latter simulations, PDLs form when sloshing motions amplify magnetic fields through shear flows (Keshet et al. 2010), reducing thermal pressure and creating low-density channels (see Figure 23 of ZuHone et al. (2011)).

In Abell 520, the observed PDL aligned with the direction of a secondary subcluster merger (Wang et al. 2016). Although Abell 2597 is a relaxed cluster with no evidence of a recent merger, simulations by ZuHone et al. (2011) show that residual sloshing motions from a past major merger can persist for several billion years and still generate PDLs. Since galaxy clusters are expected to form a dominant halo by  $z \sim 2$  ( $t_H \sim 10$  billion years) (Boylan-Kolchin et al. 2009) and subsequently grow to become the nearby clusters we see today

through mergers, lingering sloshing motions in A2597 may have played a role in forming the channel.

PDLs often form near cold fronts, given that cold fronts mark regions with particularly strong bulk motions. While the PDL in Abell 520 is observed close to a cold front, A2597 does not exhibit clear cold fronts unless we interpret the three detected surface brightness edges as such. If the edges correspond to cold fronts rather than shocks, the channel’s proximity to the inner edge would resemble the configuration in Abell 520. However, PDLs do not necessarily require an associated cold front. Preliminary results from Bellomi et al. (in prep.) show that PDLs form in seemingly random locations within the TNG Cluster simulations (Nelson et al. 2024; Truong et al. 2024).

Although we favor interpreting the channel as a PDL, its presence does not necessarily imply strong magnetic fields. Simulations by Chadayammuri et al. (2022) found that the “channel” feature observed in Abell 520 appeared both in regions with strong magnetic fields, and in purely hydrodynamic simulations without magnetic fields (see their Figures 7 and 8). Simulations by Gaspari et al. (2014) (Figure 4) also show that comparable low-density structures can emerge purely due to hydrodynamics, with turbulent eddies naturally creating alternating regions of high and low density. Therefore, without resolved measurements of the magnetic field strength in A2597, the exact origin of the channel remains uncertain.

## 6. SUMMARY

In this paper, we presented deep ( $\sim 600\text{ks}$ ) *Chandra* X-ray observations of the cool core galaxy cluster Abell 2597, complemented by archival GMRT radio data and SINFONI near-infrared observations, to study the interplay between AGN feedback, cooling, and black hole accretion. The new X-ray data provide the most detailed view to date of the cluster’s ICM, revealing both new and previously identified X-ray cavities, potential shock fronts, and a distinct surface brightness channel.

Our results are summarized as follows:

1. *Identified structures:* We identified two additional X-ray cavities, bringing the total number of cavities in the core of the cluster to six. Further out in the ICM, we detected three subtle surface brightness edges with correlated jumps in temperature, pressure, and entropy, which we interpret as potential shock fronts. Additionally, we discovered an elongated X-ray surface brightness deficit, or “channel,” which we interpret as a plasma depletion layer.

2. *Duty Cycle of the AGN*: The presence of potential shock fronts suggests that the cavities may have formed over multiple cycles of AGN activity. If this is the case, we estimate a duty cycle of  $\sim 10^7$  years, consistent with other clusters exhibiting repeated AGN feedback episodes. However, it remains possible that all the observed cavities and shocks were produced in a single, continuous AGN outburst rather than through discrete jet episodes. More detailed follow-up radio observations are needed to further distinguish between these scenarios.

### 3. *Inefficient Energy Injection from AGN Feedback*:

The cavities and potential shock fronts inject energy into the ICM at an estimated rate of  $\sim 10^{44}$  erg s $^{-1}$ , comparable to the cluster's cooling luminosity ( $L_{\text{cool}} \sim 10^{44}$  erg s $^{-1}$ ). However, this energy appears insufficient to fully counteract radiative cooling within  $r_{\text{cool}} \sim 60$  kpc, with  $< 1\%$  of the local thermal energy replaced by shock heating. The residual X-ray and UV cooling rate is just enough to fill the  $\sim 3.2 \times 10^9 M_{\odot}$  cold molecular gas reservoir near the core of the cluster, providing further evidence that AGN feedback alone does not entirely suppress cooling flows, as expected in a healthy self-regulating feedback loop.

4. *Feeding the AGN*: With an estimated Bondi power of  $P_{\text{Bondi}} \sim 2 \times 10^{43}$  erg s $^{-1}$ , an order of magnitude lower than the cavity power, hot mode accretion alone likely cannot sustain the AGN. A2597 ALMA observations of cold molecular clouds show kinematics consistent with turbulent condensation (k-plot and C-ratio diagnostics), supporting the chaotic cold accretion (CCA) scenario as the dominant feeding mechanism.

5. *The X-ray Channel*: The “channel” spans 57 kpc in length and 8 kpc in width, located near the inner surface brightness edge. It may be a plasma depletion layer, a low-density gas structure formed by sloshing-induced magnetic field amplification from a past major merger. Similar features have been observed in Abell 520 and Abell 2142, but we note their formation does not always require strong magnetic fields. Without resolved magnetic

field measurements, the channel's origin remains uncertain.

While our observations provide a detailed view of the interplay between AGN feedback and cooling in Abell 2597, several open questions concerning the precise mechanisms driving gas and metal uplift, the contributions of hot versus cold mode accretion, and the role of magnetic fields in shaping ICM structures require further exploration. Pursuing deeper, higher-resolution radio observations with the uGMRT and XRISM will be crucial for addressing these uncertainties and advancing our understanding of feedback and accretion in cool-core clusters.

## ACKNOWLEDGMENTS

The scientific results reported in this paper are based on observations from multiple ground- and space-based observatories, including the *Chandra* X-ray Observatory, the Giant Metrewave Radio Telescope (GMRT), the upgraded Giant Metrewave Radio Telescope (uGMRT), and the SINFONI near-infrared spectrograph on the Very Large Telescope (VLT).

*Chandra* data were obtained through programs supported by the Chandra X-ray Center (CXC), which is operated by the Smithsonian Astrophysical Observatory for NASA under contract NAS8-03060. The GMRT and uGMRT data were accessed through the National Centre for Radio Astrophysics (NCRA), Tata Institute of Fundamental Research (TIFR), located in Pune, India. GMRT is operated by NCRA-TIFR, and we acknowledge the significant contributions of its engineering and technical teams in making the observations possible. We also use SINFONI observations obtained at the Very Large Telescope (VLT) of the European Southern Observatory (ESO), Paranal, Chile, under program ID 0102.A-0463(A). These data were critical for mapping the distribution and kinematics of warm molecular gas in the cluster core. We acknowledge the efforts of the teams behind these facilities for enabling the collection of the high-quality data used in this work.

OO acknowledges support from the ALMA Student Observing Support grant. GRT acknowledges support for program HST-GO-16173.001-A, provided through a grant from the Space Telescope Science Institute under NASA contract NAS5-26555. MG acknowledges support from the ERC Consolidator Grant *Black-HoleWeather* (101086804).

## REFERENCES

- Allen, S. W., Dunn, R. J. H., Fabian, A. C., Taylor, G. B., & Reynolds, C. S. 2006, Monthly Notices of the Royal Astronomical Society, 372, 21, doi: [10.1111/j.1365-2966.2006.10778.x](https://doi.org/10.1111/j.1365-2966.2006.10778.x)

- Bambic, C. J., Russell, H. R., Reynolds, C. S., et al. 2023, Monthly Notices of the Royal Astronomical Society, 522, 4374, doi: [10.1093/mnras/stad824](https://doi.org/10.1093/mnras/stad824)

- Bekhti, N. B., Flöer, L., Keller, R., et al. 2016, *Astronomy & Astrophysics*, 594, A116, doi: [10.1051/0004-6361/201629178](https://doi.org/10.1051/0004-6361/201629178)
- Blanton, E. L., Randall, S. W., Clarke, T. E., et al. 2011, *The Astrophysical Journal*, 737, 99, doi: [10.1088/0004-637X/737/2/99](https://doi.org/10.1088/0004-637X/737/2/99)
- Bondi, H. 1952, *Monthly Notices of the Royal Astronomical Society*, 112, 195, doi: [10.1093/mnras/112.2.195](https://doi.org/10.1093/mnras/112.2.195)
- Bonnet, H., Strobele, S., Biancat-Marchet, F., et al. 2003, in *Adaptive Optical System Technologies II*, Vol. 4839 (SPIE), 329–343, doi: [10.1117/12.457060](https://doi.org/10.1117/12.457060)
- Bower, R. G., Benson, A. J., Malbon, R., et al. 2006, *\mnras*, 370, 645, doi: [10.1111/j.1365-2966.2006.10519.x](https://doi.org/10.1111/j.1365-2966.2006.10519.x)
- Boylan-Kolchin, M., Springel, V., White, S. D. M., Jenkins, A., & Lemson, G. 2009, *Monthly Notices of the Royal Astronomical Society*, 398, 1150, doi: [10.1111/j.1365-2966.2009.15191.x](https://doi.org/10.1111/j.1365-2966.2009.15191.x)
- Birzan, L., Rafferty, D. A., McNamara, B. R., Wise, M. W., & Nulsen, P. E. J. 2004, *The Astrophysical Journal*, 607, 800, doi: [10.1086/383519](https://doi.org/10.1086/383519)
- Chadayammuri, U., ZuHone, J., Nulsen, P., Nagai, D., & Russell, H. 2022, *Monthly Notices of the Royal Astronomical Society*, 512, 2157, doi: [10.1093/mnras/stac594](https://doi.org/10.1093/mnras/stac594)
- Churazov, E., Brüggen, M., Kaiser, C. R., Böhringer, H., & Forman, W. 2001, *\apj*, 554, 261, doi: [10.1086/321357](https://doi.org/10.1086/321357)
- Churazov, E., Sunyaev, R., Forman, W., & Böhringer, H. 2002, *\mnras*, 332, 729, doi: [10.1046/j.1365-8711.2002.05332.x](https://doi.org/10.1046/j.1365-8711.2002.05332.x)
- Clarke, T. E., Sarazin, C. L., Blanton, E. L., Neumann, D. M., & Kassim, N. E. 2005, *The Astrophysical Journal*, 625, 748, doi: [10.1086/429717](https://doi.org/10.1086/429717)
- Croton, D. J., Springel, V., White, S. D. M., et al. 2006, *Monthly Notices of the Royal Astronomical Society*, 365, 11, doi: [10.1111/j.1365-2966.2005.09675.x](https://doi.org/10.1111/j.1365-2966.2005.09675.x)
- Eisenhauer, F., Abuter, R., Bickert, K., et al. 2003, in *Instrument Design and Performance for Optical/Infrared Ground-based Telescopes*, Vol. 4841 (SPIE), 1548–1561, doi: [10.1117/12.459468](https://doi.org/10.1117/12.459468)
- Enßlin, T. A. 2001, *Astronomy & Astrophysics*, 366, 26, doi: [10.1051/0004-6361:20000198](https://doi.org/10.1051/0004-6361:20000198)
- Fabian, A. C. 2012, *Annual Review of Astronomy and Astrophysics*, 50, 455, doi: [10.1146/annurev-astro-081811-125521](https://doi.org/10.1146/annurev-astro-081811-125521)
- Fabian, A. C., Ferland, G. J., Sanders, J. S., et al. 2022, *Monthly Notices of the Royal Astronomical Society*, 515, 3336, doi: [10.1093/mnras/stac2003](https://doi.org/10.1093/mnras/stac2003)
- Fabian, A. C., Sanders, J. S., Allen, S. W., et al. 2003, *Monthly Notices of the Royal Astronomical Society*, 344, L43, doi: [10.1046/j.1365-8711.2003.06902.x](https://doi.org/10.1046/j.1365-8711.2003.06902.x)
- Fabian, A. C., Sanders, J. S., Ferland, G. J., et al. 2023, *Monthly Notices of the Royal Astronomical Society*, 524, 716, doi: [10.1093/mnras/stad1870](https://doi.org/10.1093/mnras/stad1870)
- Fabian, A. C., Sanders, J. S., Taylor, G. B., et al. 2006, *Monthly Notices of the Royal Astronomical Society*, 366, 417, doi: [10.1111/j.1365-2966.2005.09896.x](https://doi.org/10.1111/j.1365-2966.2005.09896.x)
- Freudling, W., Romaniello, M., Bramich, D. M., et al. 2013, *Astronomy & Astrophysics*, 559, A96, doi: [10.1051/0004-6361/201322494](https://doi.org/10.1051/0004-6361/201322494)
- Fruscione, A., McDowell, J. C., Allen, G. E., et al. 2006, in *Observatory Operations: Strategies, Processes, and Systems*, Vol. 6270 (SPIE), 586–597, doi: [10.1117/12.671760](https://doi.org/10.1117/12.671760)
- Gaspari, M., Brighenti, F., & Temi, P. 2015, *\aap*, 579, A62, doi: [10.1051/0004-6361/201526151](https://doi.org/10.1051/0004-6361/201526151)
- Gaspari, M., Churazov, E., Nagai, D., Lau, E. T., & Zhuravleva, I. 2014, *Astronomy & Astrophysics*, 569, A67, doi: [10.1051/0004-6361/201424043](https://doi.org/10.1051/0004-6361/201424043)
- Gaspari, M., Ruszkowski, M., & Oh, S. P. 2013, *Monthly Notices of the Royal Astronomical Society*, 432, 3401, doi: [10.1093/mnras/stt692](https://doi.org/10.1093/mnras/stt692)
- Gaspari, M., Ruszkowski, M., & Sharma, P. 2012, *The Astrophysical Journal*, 746, 94, doi: [10.1088/0004-637X/746/1/94](https://doi.org/10.1088/0004-637X/746/1/94)
- Gaspari, M., Temi, P., & Brighenti, F. 2017, *Monthly Notices of the Royal Astronomical Society*, 466, 677, doi: [10.1093/mnras/stw3108](https://doi.org/10.1093/mnras/stw3108)
- Gaspari, M., Tombesi, F., & Cappi, M. 2020, *Nature Astronomy*, 4, 10, doi: [10.1038/s41550-019-0970-1](https://doi.org/10.1038/s41550-019-0970-1)
- Gaspari, M., McDonald, M., Hamer, S. L., et al. 2018, *The Astrophysical Journal*, 854, 167, doi: [10.3847/1538-4357/aaaa1b](https://doi.org/10.3847/1538-4357/aaaa1b)
- Ginsburg, A., Sokolov, V., Val-Borro, M. d., et al. 2022, *The Astronomical Journal*, 163, 291, doi: [10.3847/1538-3881/ac695a](https://doi.org/10.3847/1538-3881/ac695a)
- Hlavacek-Larrondo, J., Fabian, A. C., Edge, A. C., et al. 2012, *Monthly Notices of the Royal Astronomical Society*, 421, 1360, doi: [10.1111/j.1365-2966.2011.20405.x](https://doi.org/10.1111/j.1365-2966.2011.20405.x)
- Hlavacek-Larrondo, J., McDonald, M., Benson, B. A., et al. 2015, *The Astrophysical Journal*, 805, 35, doi: [10.1088/0004-637X/805/1/35](https://doi.org/10.1088/0004-637X/805/1/35)
- Juráňová, A., Werner, N., Gaspari, M., et al. 2019, *Monthly Notices of the Royal Astronomical Society*, 484, 2886, doi: [10.1093/mnras/stz185](https://doi.org/10.1093/mnras/stz185)
- Keshet, U., Markevitch, M., Birnboim, Y., & Loeb, A. 2010, *The Astrophysical Journal Letters*, 719, L74, doi: [10.1088/2041-8205/719/1/L74](https://doi.org/10.1088/2041-8205/719/1/L74)
- Kirkpatrick, C. C., McNamara, B. R., Rafferty, D. A., et al. 2009, *\apj*, 697, 867, doi: [10.1088/0004-637X/697/1/867](https://doi.org/10.1088/0004-637X/697/1/867)

- Kormendy, J., & Ho, L. C. 2013, *\araa*, 51, 511, doi: [10.1146/annurev-astro-082708-101811](https://doi.org/10.1146/annurev-astro-082708-101811)
- Laha, S., Reynolds, C. S., Reeves, J., et al. 2021, *Nature Astronomy*, 5, 13, doi: [10.1038/s41550-020-01255-2](https://doi.org/10.1038/s41550-020-01255-2)
- Liu, W., Sun, M., Nulsen, P., et al. 2019, *Monthly Notices of the Royal Astronomical Society*, 484, 3376, doi: [10.1093/mnras/stz229](https://doi.org/10.1093/mnras/stz229)
- Markevitch, M., & Vikhlinin, A. 2007, *Physics Reports*, 443, 1, doi: [10.1016/j.physrep.2007.01.001](https://doi.org/10.1016/j.physrep.2007.01.001)
- McConnell, N. J., Ma, C.-P., Gebhardt, K., et al. 2011, *Nature*, 480, 215, doi: [10.1038/nature10636](https://doi.org/10.1038/nature10636)
- McCourt, M., Sharma, P., Quataert, E., & Parrish, I. J. 2012, *Monthly Notices of the Royal Astronomical Society*, 419, 3319, doi: [10.1111/j.1365-2966.2011.19972.x](https://doi.org/10.1111/j.1365-2966.2011.19972.x)
- McDonald, M., Gaspari, M., McNamara, B. R., & Tremblay, G. R. 2018, *The Astrophysical Journal*, 858, 45, doi: [10.3847/1538-4357/aabace](https://doi.org/10.3847/1538-4357/aabace)
- McNamara, B., & Nulsen, P. 2007, *Annual Review of Astronomy and Astrophysics*, 45, 117, doi: [10.1146/annurev.astro.45.051806.110625](https://doi.org/10.1146/annurev.astro.45.051806.110625)
- McNamara, B. R., & Nulsen, P. E. J. 2012, *New Journal of Physics*, 14, 055023, doi: [10.1088/1367-2630/14/5/055023](https://doi.org/10.1088/1367-2630/14/5/055023)
- McNamara, B. R., Wise, M. W., Nulsen, P. E. J., et al. 2001, *The Astrophysical Journal*, 562, L149, doi: [10.1086/338326](https://doi.org/10.1086/338326)
- Nelson, D., Pillepich, A., Ayromlou, M., et al. 2024, *Astronomy & Astrophysics*, 686, A157, doi: [10.1051/0004-6361/202348608](https://doi.org/10.1051/0004-6361/202348608)
- Nulsen, P. E. J., McNamara, B. R., Wise, M. W., & David, L. P. 2005, *The Astrophysical Journal*, 628, 629, doi: [10.1086/430845](https://doi.org/10.1086/430845)
- Oegerle, W. R., Cowie, L., Davidsen, A., et al. 2001, *The Astrophysical Journal*, 560, 187, doi: [10.1086/322246](https://doi.org/10.1086/322246)
- Olivares, V., Picquenot, A., Su, Y., et al. 2025, H\$-\$X-ray Surface Brightness Correlation for Filaments in Cooling Flow Clusters, arXiv, doi: [10.48550/arXiv.2501.01902](https://doi.org/10.48550/arXiv.2501.01902)
- Olivares, V., Salomé, P., Hamer, S. L., et al. 2022, *Astronomy & Astrophysics*, 666, A94, doi: [10.1051/0004-6361/202142475](https://doi.org/10.1051/0004-6361/202142475)
- Omoruyi, O., Tremblay, G. R., Combes, F., et al. 2023, "Beads on a String" Star Formation Tied to one of the most Powerful AGN Outbursts Observed in a Cool Core Galaxy Cluster, arXiv, doi: [10.48550/arXiv.2312.06762](https://doi.org/10.48550/arXiv.2312.06762)
- Oonk, J. B. R., Jaffe, W., Bremer, M. N., & van Weeren, R. J. 2010, *Monthly Notices of the Royal Astronomical Society*, 405, 898, doi: [10.1111/j.1365-2966.2010.16535.x](https://doi.org/10.1111/j.1365-2966.2010.16535.x)
- Panagoulia, E. K., Fabian, A. C., & Sanders, J. S. 2014, *Monthly Notices of the Royal Astronomical Society*, 438, 2341, doi: [10.1093/mnras/stt2349](https://doi.org/10.1093/mnras/stt2349)
- Pizzolato, F., & Soker, N. 2005, *\apj*, 632, 821, doi: [10.1086/444344](https://doi.org/10.1086/444344)
- Qiu, Y., Bogdanović, T., Li, Y., McDonald, M., & McNamara, B. R. 2020, *Nature Astronomy*, 4, 900, doi: [10.1038/s41550-020-1090-7](https://doi.org/10.1038/s41550-020-1090-7)
- Rafferty, D. A., McNamara, B. R., Nulsen, P. E. J., & Wise, M. W. 2006, *The Astrophysical Journal*, 652, 216, doi: [10.1086/507672](https://doi.org/10.1086/507672)
- Randall, S. W., Forman, W. R., Giacintucci, S., et al. 2010, *The Astrophysical Journal*, 726, 86, doi: [10.1088/0004-637X/726/2/86](https://doi.org/10.1088/0004-637X/726/2/86)
- Randall, S. W., Nulsen, P. E. J., Jones, C., et al. 2015, *The Astrophysical Journal*, 805, 112, doi: [10.1088/0004-637X/805/2/112](https://doi.org/10.1088/0004-637X/805/2/112)
- Rose, T., McNamara, B. R., Combes, F., et al. 2023, *Monthly Notices of the Royal Astronomical Society*, 518, 878, doi: [10.1093/mnras/stac3194](https://doi.org/10.1093/mnras/stac3194)
- Russell, H. R., Fabian, A. C., McNamara, B. R., & Broderick, A. E. 2015, *Monthly Notices of the Royal Astronomical Society*, 451, 588, doi: [10.1093/mnras/stv954](https://doi.org/10.1093/mnras/stv954)
- Russell, H. R., McNamara, B. R., Edge, A. C., et al. 2013a, *Monthly Notices of the Royal Astronomical Society*, 432, 530, doi: [10.1093/mnras/stt490](https://doi.org/10.1093/mnras/stt490)
- Russell, H. R., Sanders, J. S., Fabian, A. C., et al. 2010, *Monthly Notices of the Royal Astronomical Society*, 406, 1721, doi: [10.1111/j.1365-2966.2010.16822.x](https://doi.org/10.1111/j.1365-2966.2010.16822.x)
- Russell, H. R., McNamara, B. R., Edge, A. C., et al. 2013b, ArXiv e-prints
- Sanders, J. S. 2006, *Monthly Notices of the Royal Astronomical Society*, 371, 829, doi: [10.1111/j.1365-2966.2006.10716.x](https://doi.org/10.1111/j.1365-2966.2006.10716.x)
- Sanders, J. S., & Fabian, A. C. 2013, *Monthly Notices of the Royal Astronomical Society*, 429, 2727, doi: [10.1093/mnras/sts543](https://doi.org/10.1093/mnras/sts543)
- Sanders, J. S., Fabian, A. C., Russell, H. R., Walker, S. A., & Blundell, K. M. 2016, *Monthly Notices of the Royal Astronomical Society*, 460, 1898, doi: [10.1093/mnras/stw1119](https://doi.org/10.1093/mnras/stw1119)
- Sanders, J. S., Biffi, V., Brüggen, M., et al. 2022, *Astronomy & Astrophysics*, 661, A36, doi: [10.1051/0004-6361/202141501](https://doi.org/10.1051/0004-6361/202141501)
- Sarazin, C. 1988, X-ray Emission from Clusters of Galaxies. <http://ned.ipac.caltech.edu/level5/March02/Sarazin/frames.html>
- Schawinski, K., Koss, M., Berney, S., & Sartori, L. F. 2015, *Monthly Notices of the Royal Astronomical Society*, 451, 2517, doi: [10.1093/mnras/stv1136](https://doi.org/10.1093/mnras/stv1136)

- Sharma, P., McCourt, M., Parrish, I. J., & Quataert, E. 2012, \mnras, 427, 1219, doi: [10.1111/j.1365-2966.2012.22050.x](https://doi.org/10.1111/j.1365-2966.2012.22050.x)
- Simionescu, A., Werner, N., Böhringer, H., et al. 2009, Astronomy & Astrophysics, 493, 409, doi: [10.1051/0004-6361:200810225](https://doi.org/10.1051/0004-6361:200810225)
- Snios, B., Nulsen, P. E. J., Wise, M. W., et al. 2018, The Astrophysical Journal, 855, 71, doi: [10.3847/1538-4357/aaaf1a](https://doi.org/10.3847/1538-4357/aaaf1a)
- Sutherland, R. S., & Dopita, M. A. 1993, The Astrophysical Journal Supplement Series, 88, 253, doi: [10.1086/191823](https://doi.org/10.1086/191823)
- Sadowski, A., & Gaspari, M. 2017, Monthly Notices of the Royal Astronomical Society, 468, 1398, doi: [10.1093/mnras/stx543](https://doi.org/10.1093/mnras/stx543)
- Temi, P., Gaspari, M., Brighenti, F., et al. 2022, The Astrophysical Journal, 928, 150, doi: [10.3847/1538-4357/ac5036](https://doi.org/10.3847/1538-4357/ac5036)
- Tozzi, P., & Norman, C. 2001, The Astrophysical Journal, 546, 63, doi: [10.1086/318237](https://doi.org/10.1086/318237)
- Tremblay, G. R., O'Dea, C. P., Baum, S. A., et al. 2012a, Monthly Notices of the Royal Astronomical Society, 424, 1026, doi: [10.1111/j.1365-2966.2012.21281.x](https://doi.org/10.1111/j.1365-2966.2012.21281.x)
- Tremblay, G. R., O'Dea, C. P., Baum, S. A., et al. 2012b, Monthly Notices of the Royal Astronomical Society, 424, 1042, doi: [10.1111/j.1365-2966.2012.21278.x](https://doi.org/10.1111/j.1365-2966.2012.21278.x)
- Tremblay, G. R., Oonk, J. B. R., Combes, F., et al. 2016, Nature, 534, 218, doi: [10.1038/nature17969](https://doi.org/10.1038/nature17969)
- Tremblay, G. R., Combes, F., Oonk, J. B. R., et al. 2018, The Astrophysical Journal, 865, 13, doi: [10.3847/1538-4357/aad6dd](https://doi.org/10.3847/1538-4357/aad6dd)
- Truong, N., Pillepich, A., Nelson, D., et al. 2024, Astronomy & Astrophysics, 686, A200, doi: [10.1051/0004-6361/202348562](https://doi.org/10.1051/0004-6361/202348562)
- Ubertosi, F., Gitti, M., Brighenti, F., et al. 2023, The Astrophysical Journal, 944, 216, doi: [10.3847/1538-4357/acacf9](https://doi.org/10.3847/1538-4357/acacf9)
- Ubertosi, F., Gong, Y., Nulsen, P., et al. 2024, Cocoon shock, X-ray cavities and extended Inverse Compton emission in Hercules A: clues from Chandra observations, arXiv, doi: [10.48550/arXiv.2411.12804](https://doi.org/10.48550/arXiv.2411.12804)
- Vantyghem, A. N., McNamara, B. R., Russell, H. R., et al. 2014, Monthly Notices of the Royal Astronomical Society, 442, 3192, doi: [10.1093/mnras/stu1030](https://doi.org/10.1093/mnras/stu1030)
- Veilleux, S., Cecil, G., & Bland-Hawthorn, J. 2005, \araa, 43, 769, doi: [10.1146/annurev.astro.43.072103.150610](https://doi.org/10.1146/annurev.astro.43.072103.150610)
- Vikhlinin, A., Burenin, R., Forman, W. R., et al. 2007, in Heating versus Cooling in Galaxies and Clusters of Galaxies, ed. H. Böhringer, G. Pratt, A. Finoguenov, & P. Schuecker, Eso Astrophysics Symposia (Berlin, Heidelberg: Springer), 48–53, doi: [10.1007/978-3-540-73484-0\\_9](https://doi.org/10.1007/978-3-540-73484-0_9)
- Vikhlinin, A., Kravtsov, A., Forman, W., et al. 2006, The Astrophysical Journal, 640, 691, doi: [10.1086/500288](https://doi.org/10.1086/500288)
- Vikhlinin, A., McNamara, B. R., Forman, W., et al. 1998, The Astrophysical Journal, 502, 558, doi: [10.1086/305951](https://doi.org/10.1086/305951)
- Vikhlinin, A., Burenin, R. A., Ebeling, H., et al. 2009, The Astrophysical Journal, 692, 1033, doi: [10.1088/0004-637X/692/2/1033](https://doi.org/10.1088/0004-637X/692/2/1033)
- Voit, G. M., Cavagnolo, K. W., Donahue, M., et al. 2008, \apjl, 681, L5, doi: [10.1086/590344](https://doi.org/10.1086/590344)
- Voit, G. M., & Donahue, M. 1997, The Astrophysical Journal, 486, 242, doi: [10.1086/304509](https://doi.org/10.1086/304509)
- Wang, Q. H. S., & Markevitch, M. 2018, The Astrophysical Journal, 868, 45, doi: [10.3847/1538-4357/aae921](https://doi.org/10.3847/1538-4357/aae921)
- Wang, Q. H. S., Markevitch, M., & Giacintucci, S. 2016, The Astrophysical Journal, 833, 99, doi: [10.3847/1538-4357/833/1/99](https://doi.org/10.3847/1538-4357/833/1/99)
- Zhang, C., Zhuravleva, I., Gendron-Marsolais, M.-L., et al. 2022, Monthly Notices of the Royal Astronomical Society, 517, 616, doi: [10.1093/mnras/stac2282](https://doi.org/10.1093/mnras/stac2282)
- ZuHone, J. A., Markevitch, M., & Lee, D. 2011, The Astrophysical Journal, 743, 16, doi: [10.1088/0004-637X/743/1/16](https://doi.org/10.1088/0004-637X/743/1/16)
- Øieroset, M., Mitchell, D. L., Phan, T. D., et al. 2004, Space Science Reviews, 111, 185, doi: [10.1023/B:SPAC.0000032715.69695.9c](https://doi.org/10.1023/B:SPAC.0000032715.69695.9c)